Deformation twinning as a displacive transformation: Finite-strain phase-field model of coupled twinning and crystal plasticity

Mohsen Rezaee-Hajidehi, Przemysław Sadowski, Stanisław Stupkiewicz *

Institute of Fundamental Technological Research (IPPT), Polish Academy of Sciences, Pawińskiego 5B, 02-106 Warsaw, Poland

ARTICLE INFO

ABSTRACT

A finite-strain phase-field model of coupled deformation twinning and crystal plasticity is developed in the paper. Twinning is treated as a displacive transformation characterized by a volume-preserving stretch rather than a simple shear, the latter considered in the conventional approach. It is shown that the two approaches are equivalent in the sharp-interface description, but not in the diffuse-interface description. In the proposed stretch-based kinematics, each pair of conjugate twinning systems is represented by a single twin deformation variant, and thus a single order parameter suffices to consistently describe the two conjugate twinning systems, thereby treating them equally. The model is formulated in the framework of incremental energy minimization, which, upon time discretization, leads to a quasi-optimization problem due to the specific form of the incremental potential within the diffuse interfaces. To facilitate finite-element implementation, a micromorphic formulation of the model is employed. As an application, tensile twinning in HCP magnesium alloys is examined, and a set of comprehensive 2D plane-strain problems is studied to illustrate the features of the proposed approach.

1. Introduction

In addition to plastic slip, deformation twinning is an important inelastic deformation mechanism in metals and alloys with face-centered cubic (FCC), body-centered cubic (BCC) and hexagonal close-packed (HCP) crystal structures (Yoo and Lee, 1991; Christian and Mahajan, 1995; Gray, 2012; Beyerlein et al., 2014). In general, deformation twinning occurs in both FCC (typically, of low stacking-fault energy) and BCC metals and alloys at high strain rates or low temperatures. However, in HCP crystals, twinning is particularly common as a result of the lack of easily-activated non-basal slip systems, and is considered as a dominant deformation mechanism at room temperature, as frequently observed in experiments (e.g., Al-Samman and Gottstein, 2008; Beyerlein et al., 2010; Chapuis and Driver, 2011; Luan et al., 2018).

It is very well known that the mechanisms governing the plastic slip and deformation twinning are dissimilar in nature (Mahajan and Williams, 1973; Christian and Mahajan, 1995). Plastic slip is associated with the relative displacement of the planes of atoms with respect to each other as a result of the glide of dislocations on these planes. During twinning, a large collection of atoms undergoes a simultaneous movement such that the resulting twinned lattice is reoriented (where the reorientation is constant and occurs abruptly) and adopts a mirror symmetry with the original undeformed lattice about the twin plane. Critical differences are also discernible in the characteristics of plastic slip and deformation twinning, which lead to significant differences in the corresponding mechanical responses (Beyerlein and Arul Kumar, 2018). In particular, twinning induces a well-defined constant amount of shear and is intrinsically polarized. The latter means that, unlike the plastic slip, the activation of twin depends on the *sense* of the shear within

the twin plane. In HCP crystal, this brings on the concept of extension and contraction twin families, characterized by the c/a ratio. Another important difference is that, despite the heterogeneity of both twinning and slip, the characteristic spatial scale of twinning is by orders of magnitude larger than that of slip and is analogous to the dimensions of the polycrystalline grains (Capolungo et al., 2009; Wang et al., 2013; Beyerlein and Arul Kumar, 2018). Furthermore, the temporal scale at which the dislocation slip evolves is considerably higher compared to that of twins (Christian and Mahajan, 1995).

On account of the physical disparities discussed above, modeling the phenomenon of deformation twinning poses several additional challenges to be dealt with in comparison with the plastic slip, see Kasemer and Dawson (2020) for a related discussion, see also Roters et al. (2010). In the classical approaches based on crystal plasticity, following the seminal work of Kalidindi (1998), see also Van Houtte (1978), twinning is modeled in a mean-field sense, i.e., each twinning system is treated like an additional slip system (referred to as 'pseudo-slip') and is represented by a twin volume fraction (e.g., Agnew et al., 2001; Staroselsky and Anand, 2003; Graff et al., 2007; Kowalczyk-Gajewska, 2010; Izadbakhsh et al., 2011; Zhang and Joshi, 2012; Chang and Kochmann, 2015). The major advantages of the pseudo-slip approaches are that they are computationally inexpensive and are able to provide a reasonable prediction of the global mechanical response and the (homogenized) microstructure evolution. Nevertheless, such approaches are incapable of capturing the spatially-resolved twin morphology and, as a result, completely ignore the heterogeneous nature of the twins.

In contrast to the classical crystal-plasticity-based approaches, which are mainly relevant at the macro-scale, atomistic simulation techniques, such as molecular dynamics (MD), have gained much popularity due to the fact that they can provide valuable insights into the atomic-scale mechanisms of deformation twinning (e.g., Wang et al., 2009; Pei et al., 2018; Agarwal and Dongare, 2019). In fact, in the light of the very fast twin nucleation process, it is difficult to investigate experimentally the phenomenon of twin nucleation, the early-stage growth of the twin nuclei, and the related aspects; whereas these phenomena seem to be suitable for atomistic simulations (Capolungo and Beyerlein, 2008). On the debit side, however, atomistic techniques are restricted by the accessible spatial and temporal scales, and thereby demand large computational resources to tackle the problem of complete twin evolution. As a consequence, an intermediate (meso-scale) computational framework between the atomistic techniques and macroscopic (homogenized) approaches is needed in order to be able to resolve the morphology of the twin microstructure at adequate spatial and temporal scales.

Meso-scale modeling of twin morphology evolution has been the subject of active research in the past decade. The necessity to gain a deep understanding of the mechanisms behind the twin formation and evolution at the intra-grain and inter-grain levels and the corresponding effects on the overall mechanical behavior of materials has driven an increasing development of computational methods in this area. Notably, the phase-field method is a powerful computational tool that has found its way into the meso-scale modeling of deformation twinning. In particular, the phase-field method has been used to model the deformation twinning alone (Clayton and Knap, 2011; Liu et al., 2018b) or in combination with crystal plasticity to model the coupling between deformation twinning and dislocation slip (Kondo et al., 2014; Liu et al., 2018a; Grilli et al., 2020; Ma and Sun, 2021; Hu et al., 2021). The essence of the phase-field method is that it employs a diffuse-interface description by using an order parameter (or order parameters in the case of multiple twinning systems) that distinguishes between the matrix (untwinned) and the twinned regions and varies smoothly across the matrix–twin interface (in general, the order parameter can be conceived as the twin volume fraction, however, with a different interpretation than that in the classical crystal-plasticity-based approaches). The total free energy then comprises, in addition to the elastic strain energy, an interfacial energy contribution that is formulated in terms of the order parameter and its gradient, hence introducing an intrinsic length-scale into the model. Accordingly, the twin microstructure is described directly by the spatial distribution of the order parameter, whose evolution is governed by the classical time-dependent Ginzburg–Landau equation (Allen and Cahn, 1979), and, thereby, direct tracking of interfaces is avoided.

Apart from the phase-field method, a number of modeling approaches have been developed in recent years in an attempt to delineate the evolution of the twin microstructure at the meso-scale. In this respect, a class of models are centered around the idea of explicit incorporation of twinned domains, typically in the shape of twin plates, into the matrix (Ardeljan et al., 2015; Jin et al., 2019; Kasemer and Dawson, 2020). The main drawback of these models resides in the complexity of the solution algorithm and the associated meshing procedure, as a result of which, the presented model applications are limited only to the nucleation stage and the early-stage thickening of twin plates. In addition, extension of the models to more realistic and complex scenarios, e.g., the presence of multiple twin variants, seems to be highly intricate. Another major limitation of these models is that there is no interfacial energy, hence no intrinsic length-scale, attributed to the matrix–twin interfaces, and thus these models fail to predict the size effects. In another class of meso-scale models, twinning morphology is predicted by including the twin evolution law into the constitutive description. This list contains the micromechanics-based model of Mareau and Daymond (2016) and the complex physics-based model of Cheng et al. (2018). Modeling the twinning microstructure has been also attempted by incorporating an interaction energy term into the crystal plasticity model with the aim to penalize the simultaneous existence of the matrix and the twin (Chester et al., 2016) or by adopting a phenomenological constitutive response including softening and hardening branches that correspond to, respectively, the twin nucleation and growth stages (Qiao et al., 2016). Gradient effects are not considered by these models and also special treatments are required for the nucleation of the twin and to prevent formation of overly diffuse matrix–twin interfaces.

It appears that the phase-field method is by far the most suitable computational tool for modeling the twin microstructure evolution. Nevertheless, the application of the phase-field method in this area is still limited (the papers mentioned earlier in the context of the phase-field method are essentially the only related contributions), and thus there is a large space for further exploration. In this work, a finite-element-based model of coupled deformation twinning and plastic slip is developed via combining the phase-field method and crystal plasticity. The kinematics of the model obeys the finite-strain theory and takes into account the

reorientation induced by twinning. The model formulation and its finite-element implementation contain specific ingredients, which will be elaborated later on. Following the approach adopted by Hildebrand and Miehe (2012), see also Tůma et al. (2016, 2018), a variational structure of the model is established by casting the model into the incremental energy minimization framework.

A distinctive feature of the present model is that twinning is interpreted as a displacive transformation, as in the martensitic transformation, and, thereby, the related kinematics is formulated accordingly. More specifically, the deformation twinning is identified as a volume-preserving stretch followed by a rigid-body rotation (where the rotation is contained in the elastic part of the deformation gradient). This is in contrast to the conventional approach adopted in the literature, in which twinning is characterized by a simple shear deformation (Clayton and Knap, 2011; Kondo et al., 2014; Liu et al., 2018b; Grilli et al., 2020; Ma and Sun, 2021; Hu et al., 2021). Although the two approaches are equivalent in the sharp-interface description, they are not necessarily equivalent in the diffuse-interface description. In particular, contrary to the conventional approach, the stretch-based kinematics allows equal treatment of the conjugate twinning systems, which is particularly relevant when the conjugate twinning systems are crystallographically equivalent. These aspects are discussed extensively in Sections 2.2–2.4 and illustrated in the computational study in Section 5.2. It should be remarked here that, in the present context, the only prior application of such kinematics, see Liu et al. (2018a), pertains to the case of twinning only (without plasticity) and within the small-strain framework in which the correct orientation of the twin planes is obtained at the cost of having a compressible twinning deformation.

The remainder of this paper is structured as follows. The finite-strain kinematics of deformation twinning, in both sharp- and diffuse-interface descriptions, is presented in Section 2. To make the presentation of the model concise and comprehensible, the kinematics is customized to HCP crystals, in particular magnesium and its alloys. The variational structure of the model is presented in Section 3 and the finite-element implementation is briefly commented in Section 4. In Section 5, illustrative 2D computational studies are carried out and discussed.

2. Finite-strain kinematics of deformation twinning

2.1. Preliminaries

In this section, we discuss the finite-strain kinematics of coupled deformation twinning and crystal plasticity in sharp- and diffuse-interface descriptions. Only primary twinning is considered, which includes detwinning, i.e., reverse twinning. Secondary twinning, i.e., subsequent twinning of twinned domains, is thus not included in the analysis. Deformation twinning in HCP crystals, and in magnesium and its alloys in particular, is considered as a representative case study, however, the same concepts apply to other cases, in particular to FCC and BCC crystals, see Appendix A.

The finite-deformation framework is used throughout this work. Accordingly, the basic kinematic quantity is the deformation gradient, $\mathbf{F} = \nabla \boldsymbol{\varphi}$, which is defined as the gradient (relative to the reference configuration) of the deformation mapping $\boldsymbol{\varphi}$ that maps material points from the reference configuration to the current configuration, i.e., $\mathbf{x} = \boldsymbol{\varphi}(\mathbf{X})$, where $\mathbf{X}$ and $\mathbf{x}$ denote the positions in the respective configurations. The deformation gradient $\mathbf{F}$ is multiplicatively decomposed into the elastic part $\mathbf{F}_\mathrm{e}$ and the inelastic part $\mathbf{F}_\mathrm{in}$,

$$\mathbf{F} = \mathbf{F}_\mathrm{e} \mathbf{F}_\mathrm{in}, \qquad \mathbf{F} = \nabla \boldsymbol{\varphi} = \mathbf{I} + \nabla \mathbf{u}. \tag{1}$$

Here, $\mathbf{u} = \mathbf{x} - \mathbf{X}$ is the displacement vector, and $\mathbf{I}$ is the second-order identity tensor. The inelastic deformation described by $\mathbf{F}_\mathrm{in}$ can result from deformation twinning and from plastic slip in both the matrix and the twin. The related kinematics is discussed in detail in the following subsections.

2.2. Twinning as a displacive transformation

The $\{10\bar{1}2\}\langle\bar{1}011\rangle$ tensile twinning is an important deformation mechanism in magnesium and its alloys (Christian and Mahajan, 1995; Beyerlein et al., 2014). It involves six crystallographically-equivalent twinning systems that can be grouped into three pairs of conjugate twinning systems. A pair of conjugate twinning systems with the $(10\bar{1}2)$ and $(\bar{1}012)$ twin planes is illustrated in Fig. 1. To fix attention, the discussion below is carried out using this pair as a representative example. The main line of reasoning in this subsection, which leads to the concept of one twin deformation variant replacing two conjugate twinning systems, follows Liu et al. (2018a). Note that the kinematics described below corresponds to stress-free conditions such that $\mathbf{F}_\mathrm{e}$ in the multiplicative decomposition (1) is a rigid-body rotation, while the inelastic contribution $\mathbf{F}_\mathrm{in}$ results solely from twinning, i.e., plastic slip is absent.

Consider thus two conjugate twinning systems indexed by $i = 1, 2$. Twinning is associated with simple shear that is characterized by the deformation gradient of the form

$$\mathbf{F}_\mathrm{tw}^{(i)} = \mathbf{I} + \gamma_\mathrm{tw} \mathbf{a}^{(i)} \otimes \mathbf{m}^{(i)}, \tag{2}$$

where γ_tw is the twinning shear (Christian and Mahajan, 1995),

$$\gamma_\mathrm{tw} = \frac{\alpha^2 - 1}{\alpha} = \frac{\sqrt{3}a}{c} - \frac{c}{\sqrt{3}a}, \qquad \alpha = \frac{\sqrt{3}a}{c} > 1, \tag{3}$$
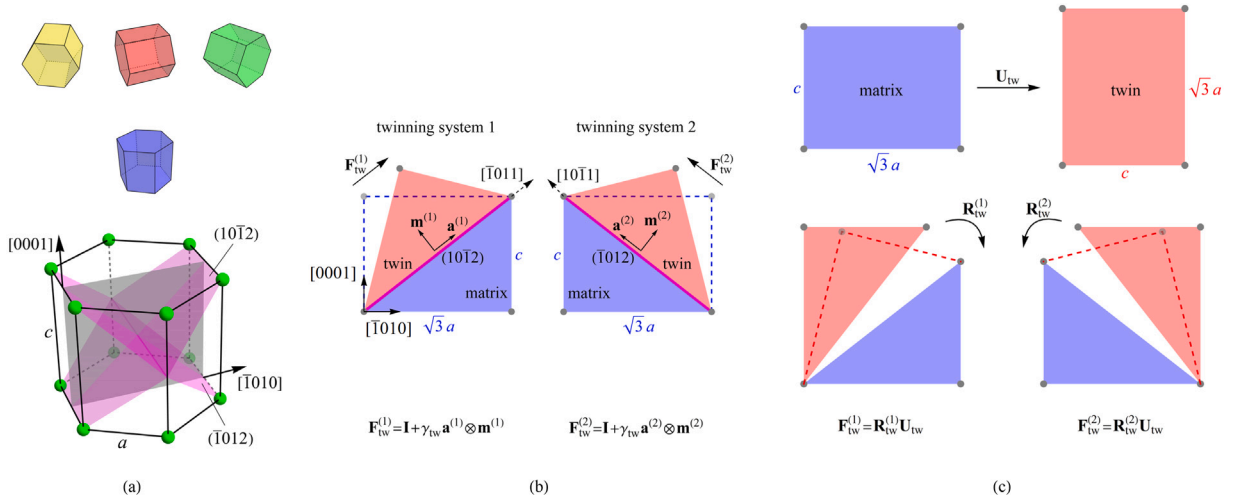
Fig. 1. Schematic illustration of the $\{10\bar{1}2\}\langle\bar{1}011\rangle$ tensile twinning in HCP crystal structure. (a) The hexagonal unit cell with the $(10\bar{1}2)$ and $(\bar{1}012)$ twin planes of two conjugate twinning systems. The small colored hexagonal unit cells represent the matrix and the three possible twin deformation variants. (b) Two conjugate twinning systems and the associated shear deformation described by $\mathbf{F}_{\text{tw}}^{(i)}$. (c) Deformation twinning interpreted as a displacive transformation involving the stretch $\mathbf{U}_{\text{tw}}$ of the matrix lattice followed by a rigid-body rotation $\mathbf{R}_{\text{tw}}^{(i)}$.

with $c/a < \sqrt{3}$ for magnesium alloys, while the unit vectors $\mathbf{m}^{(i)}$ and $\mathbf{a}^{(i)}$ specify, respectively, the twin plane normal and twinning shear direction, and $\mathbf{m}^{(i)} \cdot \mathbf{a}^{(i)} = 0$. Adopting the coordinate system with the x_1-axis along $[\bar{1}010]$ and the x_2-axis along $[0001]$, see Fig. 1, the components of vectors $\mathbf{m}^{(i)}$ and $\mathbf{a}^{(i)}$ are given by

$$\mathbf{m}^{(1,2)} = \frac{1}{\sqrt{1+\alpha^2}}(\mp 1, \alpha, 0)_{\text{C}}, \qquad \mathbf{a}^{(1,2)} = \frac{1}{\sqrt{1+\alpha^2}}(\pm\alpha, 1, 0)_{\text{C}}, \tag{4}$$

where the notation $(\cdot,\cdot,\cdot)_{\text{C}}$ is introduced to distinguish the Cartesian coordinates from the Miller indices. Note that the vectors $\mathbf{m}^{(i)}$ and $\mathbf{a}^{(i)}$ of the conjugate twin pair are perpendicular to the x_3-axis, i.e., to the $[\bar{1}2\bar{1}0]$ direction. The $(\bar{1}2\bar{1}0)$ plane is thus the plane of shear for both twins.

By applying the polar decomposition, the deformation gradient $\mathbf{F}_{\text{tw}}^{(i)}$ can be decomposed into a symmetric stretch tensor $\mathbf{U}_{\text{tw}}^{(i)}$ and a rotation (proper-orthogonal) tensor $\mathbf{R}_{\text{tw}}^{(i)}$,

$$\mathbf{F}_{\text{tw}}^{(i)} = \mathbf{R}_{\text{tw}}^{(i)}\mathbf{U}_{\text{tw}}^{(i)}. \tag{5}$$

It can be shown that the stretch tensors of two conjugate twins are equal,

$$\mathbf{U}_{\text{tw}}^{(1)} = \mathbf{U}_{\text{tw}}^{(2)} = \mathbf{U}_{\text{tw}}, \tag{6}$$

while the rotation tensors are the inverse of each other, i.e., they correspond to the rotation by the same angle but in the opposite direction,

$$\mathbf{R}_{\text{tw}}^{(1)} = \left(\mathbf{R}_{\text{tw}}^{(2)}\right)^{\text{T}} = \mathbf{R}_{\text{tw}}. \tag{7}$$

As a result, we have

$$\mathbf{F}_{\text{tw}}^{(1)} = \mathbf{R}_{\text{tw}}\mathbf{U}_{\text{tw}}, \qquad \mathbf{F}_{\text{tw}}^{(2)} = \mathbf{R}_{\text{tw}}^{\text{T}}\mathbf{U}_{\text{tw}}. \tag{8}$$

The components of $\mathbf{U}_{\text{tw}}$ and $\mathbf{R}_{\text{tw}}$ are the following,

$$\mathbf{U}_{\text{tw}} = \begin{pmatrix} \frac{1}{\alpha} & 0 & 0 \\ 0 & \alpha & 0 \\ 0 & 0 & 1 \end{pmatrix}, \qquad \mathbf{R}_{\text{tw}} = \frac{1}{1+\alpha^2}\begin{pmatrix} 2\alpha & \alpha^2-1 & 0 \\ 1-\alpha^2 & 2\alpha & 0 \\ 0 & 0 & 1+\alpha^2 \end{pmatrix}. \tag{9}$$

The stretch $\mathbf{U}_{\text{tw}}$ describes elongation by $\alpha > 1$ along the x_2-axis (i.e., the $[0001]$-axis of the crystal lattice) and contraction by $1/\alpha$ along the x_1-axis (i.e., along the $[\bar{1}010]$ direction within the basal plane), which justifies the name 'tensile twinning'. Clearly, the volume is preserved by twinning deformation, $\det \mathbf{F}_{\text{tw}}^{(i)} = \det \mathbf{U}_{\text{tw}} = 1$.

It follows that deformation twinning, which is classically identified with the shear deformation ($\mathbf{F}_{\text{in}} = \mathbf{F}_{\text{tw}}^{(i)}$ so that $\mathbf{F}_{\text{e}} = \mathbf{I}$), see Fig. 1(b), can be equivalently interpreted as a stretch ($\mathbf{F}_{\text{in}} = \mathbf{U}_{\text{tw}}$) followed by a rigid-body rotation ($\mathbf{F}_{\text{e}} = \mathbf{R}_{\text{tw}}^{(i)}$), as illustrated in Fig. 1(c). Accordingly, instead of considering the six $\{10\bar{1}2\}\langle\bar{1}011\rangle$ twinning systems, each represented by the corresponding simple shear, as in Eq. (2), it is sufficient to consider a *displacive transformation*, resembling a phase transformation, between the *matrix*

(parent phase) and three *twin deformation variants* (product phase), as schematically shown in Fig. 1(a). The rigid-body rotation is needed to preserve displacement continuity, and, for a given twin deformation variant, each of the two possible twinning planes is associated with the corresponding rotation $\mathbf{R}_{\text{tw}}^{(i)}$. The stretch tensors corresponding to the other two twin deformation variants are obtained by rotating the stretch tensor $\mathbf{U}_{\text{tw}}$ of the first twin variant, Eq. (9), by $\pm 60°$ about the [0001]-axis. It is stressed that the stretch tensors describe the overall deformation of the crystal lattice, but locally the deformation is accompanied by atomic shuffling, as in the case of the usual shear deformation (Christian and Mahajan, 1995).

Remark 2.1. The two descriptions of the kinematics of deformation twinning ($\mathbf{F}_{\text{in}} = \mathbf{F}_{\text{tw}}^{(i)}$ or $\mathbf{F}_{\text{in}} = \mathbf{U}_{\text{tw}}$) are equivalent in the sharp-interface formulation, as discussed above. However, they are no longer equivalent when the twin boundary is treated as a diffuse interface, see Remark 2.5 in Section 2.4.

Remark 2.2. As already stated, the kinematics described above corresponds to stress-free conditions. In the general case of non-zero stresses, within the twin we have

$$\mathbf{F} = \mathbf{F}_{\text{e}}\mathbf{U}_{\text{tw}} = \mathbf{F}_{\text{e}}^{*}\mathbf{F}_{\text{tw}}^{(i)}, \qquad \mathbf{F}_{\text{e}} = \mathbf{F}_{\text{e}}^{*}\mathbf{R}_{\text{tw}}^{(i)}, \tag{10}$$

where $\mathbf{F}_{\text{e}}$ and $\mathbf{F}_{\text{e}}^{*}$ are the elastic parts of the deformation gradient that correspond to the two kinematics descriptions. The two local intermediate configurations defined by $\mathbf{F}_{\text{in}} = \mathbf{F}_{\text{tw}}^{(i)}$ and $\mathbf{F}_{\text{in}} = \mathbf{U}_{\text{tw}}$ are clearly different, as they differ by a rigid-body rotation through $\mathbf{R}_{\text{tw}}^{(i)}$. However, upon adequate formulation of the elastic strain energy of the twin, including an adequate rotation of the elastic moduli tensor of the twin, the mechanical response of the twin can be shown to be invariant with respect to the choice of the intermediate configuration. This, in particular, implies that the thermodynamic driving force for propagation of an arbitrarily-oriented sharp interface separating the matrix and the twin is also invariant. The two kinematic descriptions of twinning are thus fully equivalent also in the general case of non-zero stresses. It is emphasized again that this only holds in the sharp-interface formulation, but not in the diffuse-interface formulation, as discussed in Section 2.4 and illustrated in Section 5.2.

Remark 2.3. The two twinning systems corresponding to one twin deformation variant can be found by solving the following compatibility condition,

$$\mathbf{Q}\mathbf{U}_{\text{tw}} - \mathbf{I} = \mathbf{c} \otimes \mathbf{n}, \tag{11}$$

in which the stretch $\mathbf{U}_{\text{tw}}$ is given and unknown are the rotation $\mathbf{Q}$ and vectors $\mathbf{c}$ and $\mathbf{n}$. Eq. (11) expresses the condition of displacement continuity along a planar interface of the normal $\mathbf{n}$ in stress-free conditions, i.e., a rank-one connection between the deformation gradient in the twin ($\mathbf{Q}\mathbf{U}_{\text{tw}}$) and in the matrix ($\mathbf{I}$), as in the classical crystallographic theory of martensite (Bhattacharya, 2003). Since the middle eigenvalue of $\mathbf{U}_{\text{tw}}$ is equal to one ($\lambda_2 = 1$), Eq. (11) has exactly two solutions that can be found using Proposition 4 of Ball and James (1987), see also Bhattacharya (2003). The two solutions satisfy $\mathbf{n} = \mathbf{m}^{(i)}$, $\mathbf{c} = \gamma_{\text{tw}}\mathbf{a}^{(i)}$ and $\mathbf{Q} = \mathbf{R}_{\text{tw}}^{(i)}$ for $i = 1, 2$, see Eq. (2). Note that the compatibility condition (11) can also be formulated in terms of the twinning shear $\mathbf{F}_{\text{tw}}^{(i)}$. Taking, for instance, $\mathbf{F}_{\text{tw}}^{(1)}$ with $\mathbf{m}^{(1)}$, $\mathbf{a}^{(1)}$ and γ_{tw} given, the compatibility condition reads

$$\mathbf{Q}\big(\mathbf{I} + \gamma_{\text{tw}}\mathbf{a}^{(1)} \otimes \mathbf{m}^{(1)}\big) - \mathbf{I} = \mathbf{c} \otimes \mathbf{n}. \tag{12}$$

This equation also has two solutions. One solution is trivial ($\mathbf{Q} = \mathbf{I}$, $\mathbf{n} = \mathbf{m}^{(1)}$, $\mathbf{c} = \gamma_{\text{tw}}\mathbf{a}^{(1)}$) and the second solution gives $\mathbf{Q} = \big(\mathbf{R}_{\text{tw}}^{(2)}\big)^2 = \mathbf{R}_{\text{tw}}^{-2}$, $\mathbf{n} = \mathbf{m}^{(2)}$ and $\mathbf{c} = \gamma_{\text{tw}}\mathbf{a}^{(2)}$, so that the second solution retrieves the other twinning shear, $\mathbf{F}_{\text{tw}}^{(2)}$. In particular, the following relationship holds: $\mathbf{F}_{\text{tw}}^{(2)} = \mathbf{R}_{\text{tw}}^{-2}\mathbf{F}_{\text{tw}}^{(1)}$.

2.3. Twinning and crystal plasticity

Within a continuum sharp-interface framework, the matrix–twin interface has a zero thickness, and thus each material point belongs either to matrix or to twin. Plastic deformation in the matrix (prior to twinning) is then described by the standard crystal plasticity theory (Hill and Rice, 1972; Asaro, 1983), and the corresponding deformation gradient $\mathbf{F}_{\text{m}}$ is the only contribution to the inelastic deformation gradient $\mathbf{F}_{\text{in}}$,

$$\mathbf{F}_{\text{in}} = \mathbf{F}_{\text{m}}, \qquad \dot{\mathbf{F}}_{\text{m}}\mathbf{F}_{\text{m}}^{-1} = \sum_{s=1}^{n_s} \dot{\gamma}_{\text{m}}^{s}\mathbf{s}_{\text{m}}^{s} \otimes \mathbf{n}_{\text{m}}^{s}, \tag{13}$$

where the unit vectors $\mathbf{s}_{\text{m}}^{s}$ and $\mathbf{n}_{\text{m}}^{s}$ denote, respectively, the slip direction and the slip-plane normal associated with the slip system s within the matrix, $\dot{\gamma}_{\text{m}}^{s}$ is the corresponding slip rate, and n_s denotes the number of slip systems.

Once a material point is transformed to a twin, which corresponds to a (zero-thickness) twin boundary passing through this point, its crystallographic lattice undergoes twinning deformation. As discussed in the previous subsection, the respective deformation gradient $\mathbf{F}_{\text{tw}}$ can be adopted in the form of either shear deformation, $\mathbf{F}_{\text{tw}} = \mathbf{F}_{\text{tw}}^{(i)}$, or stretch, $\mathbf{F}_{\text{tw}} = \mathbf{U}_{\text{tw}}$, see Eq. (10), the latter approach being advocated in this work. Henceforth, the prior plastic deformation in the matrix is frozen (i.e., $\dot{\mathbf{F}}_{\text{m}} = \mathbf{0}$) and further plastic deformation is realized by the plastic slip in the twin. The total inelastic deformation gradient $\mathbf{F}_{\text{in}}$ takes then the following form (Levitas, 1998; Homayonifar and Mosler, 2012),

$$\mathbf{F}_{\text{in}} = \mathbf{F}_{\text{p}}\mathbf{F}_{\text{tw}}\mathbf{F}_{\text{m}}, \qquad \dot{\mathbf{F}}_{\text{p}}\mathbf{F}_{\text{p}}^{-1} = \sum_{s=1}^{n_s} \dot{\gamma}_{\text{p}}^{s}\mathbf{s}_{\text{p}}^{s} \otimes \mathbf{n}_{\text{p}}^{s}, \qquad \mathbf{F}_{\text{tw}} = \mathbf{U}_{\text{tw}}, \qquad \dot{\mathbf{F}}_{\text{m}} = \mathbf{0}, \tag{14}$$
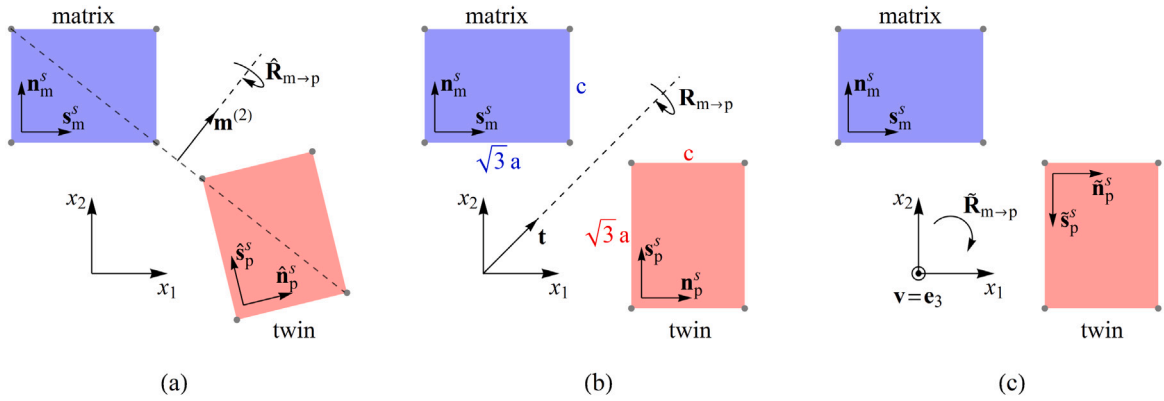
Fig. 2. Rotations relating slip systems in the matrix and in the twin: (a) the classical approach, i.e., rotation by 180° about $\mathbf{m}^{(2)}$, (b) rotation by 180° about $\mathbf{t} = \mathbf{t}^{(2)}$, (c) rotation by $-90°$ about $\mathbf{v}$.
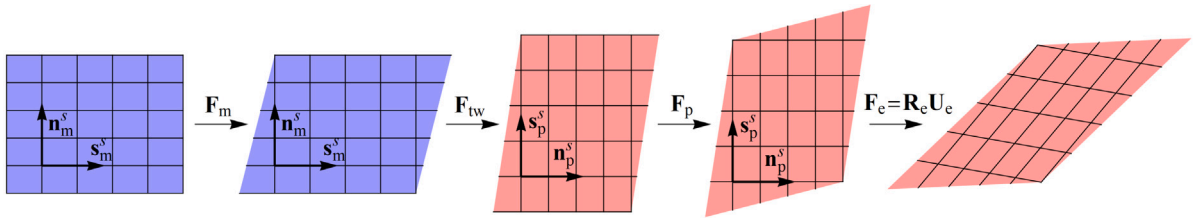

Fig. 3. Illustration of the isoclinic configuration in the case of twinning transformation.

where the slip system in the twin is specified by $\mathbf{s}_p^s$ and $\mathbf{n}_p^s$, and $\dot{\gamma}_p^s$ is the corresponding slip rate (subscript 'p' stands for 'product').

Vectors $\mathbf{s}_p^s$ and $\mathbf{n}_p^s$ are obtained by applying to, respectively, $\mathbf{s}_m^s$ and $\mathbf{n}_m^s$ a 180° rotation about the vector $\mathbf{t} = \mathbf{t}^{(i)}$ that is oriented at 45° with respect to the basal plane,

$$\mathbf{s}_p^s = \mathbf{R}_{m \to p} \mathbf{s}_m^s, \qquad \mathbf{n}_p^s = \mathbf{R}_{m \to p} \mathbf{n}_m^s, \qquad \mathbf{R}_{m \to p} = \mathbf{R}(\pi, \mathbf{t}) = 2\mathbf{t} \otimes \mathbf{t} - \mathbf{I}, \tag{15}$$

where $\mathbf{R}_{m \to p}$ is the corresponding rotation tensor, $\mathbf{t}^{(1)} = \frac{\sqrt{2}}{2}(-1, 1, 0)_C$ and $\mathbf{t}^{(2)} = \frac{\sqrt{2}}{2}(1, 1, 0)_C$. Note that the rotation by 180° about the vector $\mathbf{t}$, as specified by the tensor $\mathbf{R}_{m \to p}$, transforms the hexagonal unit cell of the matrix to that of the twin, see the sketch in Fig. 2(b). Moreover, as illustrated in Fig. 2(c), the two unit cells are also related by a $\pm90°$ rotation about vector $\mathbf{v} = (0, 0, 1)_C$, so that the corresponding rotation tensor $\tilde{\mathbf{R}}_{m \to p} = \mathbf{R}(\pm\pi/2, \mathbf{v})$ also defines an equivalent set of slip systems in the twin. The related possible difference in the sign of the vectors specifying the slip systems (e.g., compare $\mathbf{s}_p^s$ in Fig. 2(b) and $\tilde{\mathbf{s}}_p^s$ in Fig. 2(c)) has no influence, since it can be accommodated by a change in the sign of the slip rate $\dot{\gamma}_p^s$.

The kinematics specified by the multiplicative decomposition of $\mathbf{F}_{in}$ in Eq. (14)$_1$ is consistent with the classical concept of isoclinic intermediate local configuration, as illustrated in Fig. 3. The lattice is not distorted by the plastic slip in the matrix (prior to twinning) and in the twin (after twinning) so that the vectors specifying the slip systems do not change in the course of plastic deformation. During the twinning transformation, the lattice of the matrix is transformed to that of the twin through the twinning stretch $\mathbf{U}_{tw}$, and this is accompanied by the transformation of the slip systems, see Eq. (15) and the succeeding discussion. It is stressed that the rigid-body rotation is contained in the elastic deformation gradient, $\mathbf{F}_e = \mathbf{R}_e \mathbf{U}_e$, which is a part of the solution of the problem.

In the discussion above, it has been tacitly assumed that only one twin deformation variant may appear at a given material point. This is a viable assumption in the sharp-interface description, but not necessarily in the diffuse-interface description which is discussed in the next subsection.

Remark 2.4. In the classical approach, in which $\mathbf{F}_{tw} = \mathbf{F}_{tw}^{(i)}$ is used in Eq. (14), vectors $\hat{\mathbf{s}}_p^s$ and $\hat{\mathbf{n}}_p^s$ defining the slip systems in the twin are obtained by rotating those in the matrix through a 180° rotation about the twin plane normal $\mathbf{m}^{(i)}$, see Fig. 2(a),

$$\hat{\mathbf{s}}_p^s = \hat{\mathbf{R}}_{m \to p} \mathbf{s}_m^s, \qquad \hat{\mathbf{n}}_p^s = \hat{\mathbf{R}}_{m \to p} \mathbf{n}_m^s, \qquad \hat{\mathbf{R}}_{m \to p} = \mathbf{R}(\pi, \mathbf{m}^{(i)}). \tag{16}$$

If the two conjugate twinning systems are treated as independent, the respective slip systems should be defined separately for each twinning system. Note that the two descriptions, i.e., the slip systems in the twin defined by Eq. (15) and by Eq. (16), are in fact equivalent. Indeed, the following identity holds,

$$\mathbf{R}(\pi, \mathbf{m}^{(i)}) = \mathbf{R}_{tw}^{(i)} \mathbf{R}(\pi, \mathbf{t}^{(i)}), \tag{17}$$

which, in particular, implies that the slip systems $(\mathbf{s}_p^s, \mathbf{n}_p^s)$ and $(\hat{\mathbf{s}}_p^s, \hat{\mathbf{n}}_p^s)$ are rotated with respect to each other by the rotation tensor $\mathbf{R}_{tw}^{(i)}$, i.e., $\hat{\mathbf{s}}_p^s = \mathbf{R}_{tw}^{(i)}\mathbf{s}_p^s$ and $\hat{\mathbf{n}}_p^s = \mathbf{R}_{tw}^{(i)}\mathbf{n}_p^s$. Then, in analogy to Eq. (10), we have

$$\mathbf{F} = \mathbf{F}_e\mathbf{F}_p\mathbf{U}_{tw}\mathbf{F}_m = \mathbf{F}_e^*\mathbf{F}_p^*\mathbf{F}_{tw}^{(i)}\mathbf{F}_m, \qquad \mathbf{F}_e = \mathbf{F}_e^*\mathbf{R}_{tw}^{(i)}, \qquad \mathbf{F}_p = \left(\mathbf{R}_{tw}^{(i)}\right)^T\mathbf{F}_p^*\mathbf{R}_{tw}^{(i)}, \tag{18}$$

where $\mathbf{F}_p^*$ is defined in terms of $(\hat{\mathbf{s}}_p^s, \hat{\mathbf{n}}_p^s)$, as in Eq. (14). It can also be shown that the resolved shear stresses on the individual slip systems in the twin (to be discussed in Section 3.2) are identical in the two formulations.

2.4. Diffuse-interface description

In the phase-field method, the twinning plane is treated as a diffuse interface. A continuous order parameter η, where $0 \leq \eta \leq 1$, is thus introduced such that $\eta = 0$ represents the matrix, $\eta = 1$ represents the twin, and $0 < \eta < 1$ represents a diffuse matrix–twin interface. The strain due to twinning is then continuously interpolated within the diffuse interface. In the case of twinning only, i.e., when $\mathbf{F}_{in} = \mathbf{F}_{tw}$, the following logarithmic mixing rule (Tůma et al., 2016) can be adopted,

$$\mathbf{F}_{tw}(\eta) = \exp(\eta \log \mathbf{U}_{tw}), \qquad \dot{\mathbf{F}}_{tw}\mathbf{F}_{tw}^{-1} = \dot{\eta}\log\mathbf{U}_{tw}. \tag{19}$$

Note that the logarithmic mixing rule (19) guarantees that twinning deformation is incompressible, $\det\mathbf{F}_{tw} = 1$, for $0 \leq \eta \leq 1$, while this property does not hold for the popular linear mixing rule, $\mathbf{F}_{tw} = (1-\eta)\mathbf{I} + \eta\mathbf{U}_{tw}$ (Levitas and Preston, 2005), see also the related discussion on the interface stresses (Basak and Levitas, 2017).

Consider now the general case of twinning and plasticity. Since the diffuse matrix–twin interface is treated as a mixture of the two "phases", the inelastic deformation gradient $\mathbf{F}_{in}$ must comprise the contributions of plastic deformation both in the matrix and in the twin, for instance, in the following form,

$$\mathbf{L}_{in} = \dot{\mathbf{F}}_{in}\mathbf{F}_{in}^{-1} = (1-\eta)\sum_{s=1}^{n_s}\dot{\gamma}_m^s\mathbf{s}_m^s \otimes \mathbf{n}_m^s + \eta\sum_{s=1}^{n_s}\dot{\gamma}_p^s\mathbf{s}_p^s \otimes \mathbf{n}_p^s + \dot{\eta}\log\mathbf{U}_{tw}. \tag{20}$$

Here, the individual plastic-slip contributions, cf. Eqs. (13) and (14), are weighted by the respective fractions taken linear in η, while the last term is the contribution of twinning in the form resulting from the logarithmic mixing rule (19). Clearly, the flow rule (20) is consistent with those in Eqs. (13) and (14) for $\eta = 0$ and $\eta = 1$, respectively.

Formulae for the inelastic velocity gradient $\mathbf{L}_{in}$ resembling that in Eq. (20) (or, analogously, for the total plastic strain rate in the small-strain theory) can be found in several phase-field models of twinning and plasticity (Kondo et al., 2014; Liu et al., 2018b; Grilli et al., 2020; Hu et al., 2021; Ma and Sun, 2021), as well as in numerous meso-scale crystal plasticity formulations in which twinning is treated as a pseudo-slip system (e.g., Kalidindi, 1998; Staroselsky and Anand, 2003; Kowalczyk-Gajewska, 2010; Izadbakhsh et al., 2011; Zhang and Joshi, 2012; Chang and Kochmann, 2015). The difference with respect to all these formulations, and the distinctive feature of the present model, is the form of the twinning contribution in Eq. (20), which is a consequence of treating the twinning as a displacive transformation characterized by the stretch $\mathbf{U}_{tw}$, as discussed in Sections 2.2 and 2.3. It is also stressed that the slip systems in the twin are here defined by Eq. (15), so that the twinning rotation $\mathbf{R}_{tw}^{(i)}$ is not included in the kinematics of $\mathbf{F}_{in}$, as illustrated in Figs. 2 and 3. All this allows us to use a *single* twin deformation variant with the corresponding single set of slip systems to consistently represent *two* conjugate twinning systems, each involving the respective set of slip systems defined by Eq. (16). Importantly, only one order parameter is here sufficient to represent two conjugate slip systems. Generalization of Eq. (20) to the case of three twin deformation variants is immediate and is omitted here for brevity.

Remark 2.5. A popular choice for the mixing rule, as an alternative to Eq. (19), is the rank-one mixing rule defined in terms of one of the twinning systems (here, $i = 1$ to fix the attention),

$$\mathbf{F}_{tw}(\eta) = \mathbf{I} + \eta\gamma_{tw}\mathbf{a}^{(1)} \otimes \mathbf{m}^{(1)}, \tag{21}$$

which has been employed in phase-field models for twinning only (Clayton and Knap, 2011) and for twinning with plasticity (Kondo et al., 2014; Liu et al., 2018b; Ma and Sun, 2021; Hu et al., 2021). By construction, the rank-one mixing rule (21) ensures a compatible planar diffuse matrix–twin interface with the normal $\mathbf{m}^{(1)}$ for all $0 \leq \eta \leq 1$. However, for $0 < \eta < 1$, $\mathbf{F}_{tw}(\eta)$ defined by Eq. (21) does not satisfy the compatibility condition for the matrix–twin interface with the normal $\mathbf{m}^{(2)}$ (i.e., the condition $\mathbf{QF}_{tw}(\eta) - \mathbf{I} = \mathbf{c} \otimes \mathbf{m}^{(2)}$, cf. Eq. (12), is not satisfied for any $\mathbf{Q}$ and $\mathbf{c}$), and thus elastic strains are needed to accommodate the related incompatibility. As a result, formation of the two interfaces may not be energetically equivalent, see the related discussion in Section 5.2. A possible workaround is to use two order parameters, one for each twinning system, which is, however, associated with an additional computational cost and would be particularly pronounced in the 3D setting with 6 twinning systems in HCP crystals and 12 twinning systems in FCC and BBC crystals. In the case of the logarithmic mixing rule (19), the two twinning systems are treated equivalently. However, none of the corresponding diffuse interfaces is perfectly compatible so that the incompatibility must be accommodated by elastic strains. As shown in Section 5.2, in terms of incompatibility and overall energy of interfaces, the logarithmic mixing rule (19) can be considered an intermediate case between the two twinning systems treated by the rank-one mixing rule (21).

Remark 2.6. It has been observed in experiments that interaction of two conjugate twins leads to formation of a twin–twin boundary which is a low-angle tilt boundary (Yu et al., 2014). One of the consequences of using a single order parameter to represent two conjugate twins is that such a twin–twin boundary is not represented by a genuine interface once the matrix–twin interfaces of the two conjugate twins annihilate and the order parameter becomes thus constant within the single "twin phase" formed by the two twins. The results reported in Section 5.5, see Fig. 20 and the corresponding discussion, show that the twin–twin boundary is then represented by a steep gradient of the lattice orientation angle, which can be interpreted as a low-angle tilt boundary in a diffuse form, consistent with the phase-field framework. However, such a boundary cannot be controlled in terms of its energy and mobility, which is a limitation of the present approach.

Remark 2.7. The proposed stretch-based kinematics treats the two conjugate twinning systems equally, as discussed in Remark 2.5. Accordingly, this approach is particularly suitable for those twinning modes in which the conjugate twinning systems are crystallographically equivalent, in particular, for the $\{10\bar{1}2\}\langle\bar{1}011\rangle$ twinning mode in HCP crystals (studied in detail in this paper) and also for the $\{111\}\langle11\bar{2}\rangle$ twinning mode in FCC crystals and $\{112\}\langle\bar{1}\bar{1}1\rangle$ twinning mode in BCC crystals that are briefly commented in Appendix A. When the conjugate twining systems are not crystallographically equivalent, both in high- and low-symmetry crystals, they may be characterized by different interfacial energies and interface mobilities, and this should be accounted for in the corresponding phase-field description.

Remark 2.8. Eq. (20) is not the only option to define $\mathbf{F}_{\text{in}}$ in the diffuse-interface framework. In principle, the multiplicative decomposition (14)$_1$ can be used directly, provided that the components $\mathbf{F}_{\text{m}}$, $\mathbf{F}_{\text{tw}}$ and $\mathbf{F}_{\text{p}}$ are integrated individually. This is particularly simple in the case of single slip, i.e., when only one slip system is considered in the matrix and in the twin, so that $\mathbf{F}_{\text{in}}$ can be written in an explicit form,

$$\mathbf{F}_{\text{in}}(\eta, \tilde{\gamma}_{\text{m}}, \tilde{\gamma}_{\text{p}}) = \mathbf{F}_{\text{p}}(\tilde{\gamma}_{\text{p}})\mathbf{F}_{\text{tw}}(\eta)\mathbf{F}_{\text{m}}(\tilde{\gamma}_{\text{m}}). \tag{22}$$

Here, $\mathbf{F}_{\text{tw}}$ is defined by Eq. (19)$_1$, while the plastic deformation in the matrix, described by $\mathbf{F}_{\text{m}}$, is defined in terms of the effective slip $\tilde{\gamma}_{\text{m}}$ on slip system $(\mathbf{s}_{\text{m}}, \mathbf{n}_{\text{m}})$, and likewise $\mathbf{F}_{\text{p}}$ in the twin is defined in terms of $\tilde{\gamma}_{\text{p}}$ and $(\mathbf{s}_{\text{p}}, \mathbf{n}_{\text{p}})$,

$$\mathbf{F}_{\text{m}}(\tilde{\gamma}_{\text{m}}) = \mathbf{I} + \tilde{\gamma}_{\text{m}}\mathbf{s}_{\text{m}} \otimes \mathbf{n}_{\text{m}}, \qquad \mathbf{F}_{\text{p}}(\tilde{\gamma}_{\text{p}}) = \mathbf{I} + \tilde{\gamma}_{\text{p}}\mathbf{s}_{\text{p}} \otimes \mathbf{n}_{\text{p}}, \tag{23}$$

where the effective slips are governed by

$$\dot{\tilde{\gamma}}_{\text{m}} = (1-\eta)\dot{\gamma}_{\text{m}}, \qquad \dot{\tilde{\gamma}}_{\text{p}} = \eta\dot{\gamma}_{\text{p}}. \tag{24}$$

A brief discussion regarding the kinematic assumption specified by Eqs. (22)–(24) is provided in Section 5.3.

3. Variational formulation of the model

In this section, a variational formulation of the phase-field model of deformation twinning is developed by following the approach of Hildebrand and Miehe (2012), see also Tůma et al. (2016, 2018). The approach is here extended to include crystal plasticity as an additional mechanism of inelastic deformation, and a micromorphic regularization is employed to facilitate finite-element implementation of the model (Forest, 2009; Rezaee-Hajidehi and Stupkiewicz, 2021).

3.1. Free energy function and micromorphic regularization

The elastic strain energy ψ_{e}, the stored plastic energy ψ_{h}, and the (interfacial) energy of twin boundaries ψ_{Γ} constitute the components of the (isothermal) total free energy ψ, i.e.,

$$\psi(\mathbf{F}, \mathbf{F}_{\text{in}}, \bar{\gamma}, \eta, \nabla\eta) = \psi_{\text{e}}(\mathbf{F}_{\text{e}}, \eta) + \psi_{\text{h}}(\bar{\gamma}) + \psi_{\Gamma}(\eta, \nabla\eta) + I_{[0,1]}(\eta), \tag{25}$$

where $\mathbf{F}_{\text{e}} = \mathbf{F}\mathbf{F}_{\text{in}}^{-1}$, and $\bar{\gamma}$ is the accumulated plastic slip with the following evolution law,

$$\dot{\bar{\gamma}} = (1-\eta)\sum_{s=1}^{n_{\text{s}}}|\dot{\gamma}_{\text{m}}^{s}| + \eta\sum_{s=1}^{n_{\text{s}}}|\dot{\gamma}_{\text{p}}^{s}|. \tag{26}$$

In order to account for the inequality constraints on the order parameter, $0 \leq \eta \leq 1$, the indicator function $I_{[0,1]}$ is included in Eq. (25) and is expressed as

$$I_{[0,1]}(\eta) = \begin{cases} 0 & \text{if } 0 \leq \eta \leq 1, \\ +\infty & \text{otherwise.} \end{cases} \tag{27}$$

Next, we specify the individual components of the total free energy. The elastic strain energy ψ_{e} is expressed as

$$\psi_{\text{e}}(\mathbf{F}_{\text{e}}, \eta) = \frac{1}{2}\mathbf{H}_{\text{e}} \cdot \mathbb{L}(\eta)\mathbf{H}_{\text{e}}, \qquad \mathbf{H}_{\text{e}} = \frac{1}{2}\log(\mathbf{C}_{\text{e}}), \qquad \mathbf{C}_{\text{e}} = \mathbf{F}_{\text{e}}^{\text{T}}\mathbf{F}_{\text{e}}, \tag{28}$$

where $\mathbf{H}_{\text{e}}$ is the logarithmic elastic strain, and $\mathbb{L}(\eta) = (1-\eta)\mathbb{L}_{\text{m}} + \eta\mathbb{L}_{\text{p}}$ is the fourth-order elastic stiffness tensor. Here, $\mathbb{L}_{\text{m}}$ is the elastic stiffness tensor of the matrix (transversely isotropic in the case of an HCP crystal) and $\mathbb{L}_{\text{p}}$ is that of the twin, which can be

obtained by applying the rotation $\mathbf{R}_{m\to p}$ to $\mathbb{L}_m$ (i.e., $\mathbb{L}_p = \mathbf{R}_{m\to p}\circ\mathbb{L}_m$), see Section 2.3. The Hencky-type anisotropic elastic strain energy (28) behaves well in a much wider range of strains than the popular St. Venant–Kirchhoff energy (Rezaee-Hajidehi et al., 2021). However, its practical application, specifically calculation of the stress and the tangent operator, requires computation of the first and second derivatives of the tensor logarithm, which is not straightforward. The closed-form representation of the matrix logarithm (Hudobivnik and Korelc, 2016) is used here for this purpose, see Section 4.

The stored plastic energy ψ_h that accounts for the hardening behavior is written as

$$\psi_h(\bar{\gamma}) = \frac{1}{2}H\bar{\gamma}^2, \tag{29}$$

where H is the hardening parameter. This form of ψ_h corresponds to a simple linear (isotropic) hardening which is adopted here for simplicity.

The energy of the twin boundaries ψ_Γ, assumed here isotropic, is formulated in terms of the order parameter η and its gradient $\nabla\eta$, i.e.,

$$\psi_\Gamma(\eta, \nabla\eta) = \Delta f \eta(1-\eta) + \kappa\nabla\eta\cdot\nabla\eta, \tag{30}$$

where the parameters Δf and κ characterize, respectively, the height of the energy barrier for the formation of the twin interface and the gradient energy associated with the twin interface and are defined as

$$\Delta f = \frac{4\Gamma}{\pi\ell}, \qquad \kappa = \frac{4\Gamma\ell}{\pi}, \tag{31}$$

where Γ is the interfacial energy density (per unit area) and ℓ is the interface thickness parameter. In the case of the so-called double-obstacle potential specified by Eq. (30), the theoretical interface thickness is equal to $\pi\ell$ (Steinbach, 2009; Tůma et al., 2018).

We now reformulate the total free energy density in the framework of the micromorphic approach. This general approach (and its name) is adopted after Forest (2009), and its application to the phase-field method follows Rezaee-Hajidehi and Stupkiewicz (2021). As will be shown in the sequel, the micromorphic regularization facilitates the finite-element implementation of the model. In this approach, a new variable χ is introduced into the model and is enforced to be close to the order parameter η through a penalty term. The new form of the total free energy, ψ_μ, now reads

$$\psi_\mu(\mathbf{F}, \mathbf{F}_{in}, \bar{\gamma}, \eta, \chi, \nabla\chi) = \psi_e(\mathbf{F}_e, \eta) + \psi_h(\bar{\gamma}) + \psi_\Gamma(\eta, \nabla\chi) + \psi_{pen}(\eta, \chi) + I_{[0,1]}(\eta), \tag{32}$$

where the term ψ_{pen} penalizes the discrepancy between η and χ and is expressed as

$$\psi_{pen}(\eta, \chi) = \frac{1}{2}\epsilon_\mu(\eta - \chi)^2, \tag{33}$$

with ϵ_μ as the micromorphic penalty parameter. According to Eq. (32), upon the micromorphic regularization, the interfacial energy of twin boundaries, ψ_Γ, is expressed in terms of the gradient of the micromorphic variable $\nabla\chi$ instead of $\nabla\eta$, i.e., $\psi_\Gamma(\eta, \nabla\chi) = \Delta f\eta(1-\eta) + \kappa\nabla\chi\cdot\nabla\chi$.

The indicator function $I_{[0,1]}$ imposing the bound constraints on η in Eq. (32) is not differentiable. In the following derivations, we approximate $I_{[0,1]}$ by a regularized indicator function $I_{[0,1]}^\epsilon$ that is convex and continuously differentiable and depends on a regularization parameter ϵ such that, in the limit $\epsilon \to \infty$, the regularized indicator function $I_{[0,1]}^\epsilon$ converges to $I_{[0,1]}$. This replacement is made in order to simplify the subsequent derivations only, as the related aspects are not crucial here. Note, however, that in the actual finite-element implementation of the model, the inequality constraints are imposed exactly by using the augmented Lagrangian method, see the discussion in Section 4.

3.2. Formulation of the rate-problem

Considering that the free energy ψ_μ depends on $\mathbf{F}$ and $\mathbf{F}_{in}$ only through $\mathbf{F}_e = \mathbf{F}\mathbf{F}_{in}^{-1}$ in ψ_e, cf. Eq. (32), the rate of change of ψ_μ can be expressed as

$$\dot{\psi}_\mu = \frac{\partial\psi_e}{\partial\mathbf{F}_e}\cdot\dot{\mathbf{F}}_e + \frac{\partial\psi_\mu}{\partial\bar{\gamma}}\dot{\bar{\gamma}} + \frac{\partial\psi_\mu}{\partial\eta}\dot{\eta} + \frac{\partial\psi_\mu}{\partial\chi}\dot{\chi} + \frac{\partial\psi_\mu}{\partial\nabla\chi}\cdot\nabla\dot{\chi}, \qquad \dot{\mathbf{F}}_e = \dot{\mathbf{F}}\mathbf{F}_{in}^{-1} - \mathbf{F}_e\mathbf{L}_{in}. \tag{34}$$

The first term in Eq. $(34)_1$ can be transformed, in the standard manner, to

$$\frac{\partial\psi_e}{\partial\mathbf{F}_e}\cdot\dot{\mathbf{F}}_e = \left(\mathbf{P}\mathbf{F}_{in}^T\right)\cdot\dot{\mathbf{F}}_e = \mathbf{P}\cdot\dot{\mathbf{F}} - \mathbf{M}\cdot\mathbf{L}_{in}, \tag{35}$$

where $\mathbf{P} = \partial\psi_\mu/\partial\mathbf{F} = J\boldsymbol{\sigma}\mathbf{F}^{-T}$ is the first Piola–Kirchhoff stress tensor, $\mathbf{M} = \mathbf{F}_e^T\mathbf{P}\mathbf{F}_{in}^T = J\mathbf{F}_e^T\boldsymbol{\sigma}\mathbf{F}_e^{-T}$ is the (nonsymmetric) Mandel stress, $\boldsymbol{\sigma}$ is the Cauchy stress and $J = \det\mathbf{F}$.

Eq. (34) together with the evolution rules for $\mathbf{F}_{in}$, Eq. (20), and for $\bar{\gamma}$, Eq. (26), indicate the dependence of $\dot{\psi}_\mu$ on the rate quantities $(\dot{\mathbf{F}}, \dot{\boldsymbol{\gamma}}, \dot{\eta}, \dot{\chi}, \nabla\dot{\chi})$, where the vector $\dot{\boldsymbol{\gamma}} = \{\dot{\boldsymbol{\gamma}}_m, \dot{\boldsymbol{\gamma}}_p\}$ gathers the slip rates associated with the matrix and the twin, $\dot{\boldsymbol{\gamma}}_m = \{\dot{\gamma}_m^1, \dot{\gamma}_m^2, \ldots, \dot{\gamma}_m^{n_s}\}$ and $\dot{\boldsymbol{\gamma}}_p = \{\dot{\gamma}_p^1, \dot{\gamma}_p^2, \ldots, \dot{\gamma}_p^{n_s}\}$. To shorten the notation, whenever it is more convenient, the rate quantities $(\dot{\mathbf{F}}, \dot{\boldsymbol{\gamma}}, \dot{\eta}, \dot{\chi}, \nabla\dot{\chi})$ are collectively referred to as $\dot{\mathfrak{h}}$,

$$\dot{\mathfrak{h}} = \{\dot{\mathbf{F}}, \dot{\boldsymbol{\gamma}}, \dot{\eta}, \dot{\chi}, \nabla\dot{\chi}\}, \tag{36}$$

so that $\dot{\psi}_\mu(\dot{\mathbf{F}}, \dot{\bar{\gamma}}, \dot{\eta}, \dot{\chi}, \nabla\dot{\chi})$ and $\dot{\psi}_\mu(\dot{\mathfrak{h}})$ can be used interchangeably. Here, the dependence of ψ_μ on the state variables $(\mathbf{F}, \mathbf{F}_{\text{in}}, \bar{\gamma}, \eta, \chi, \nabla\chi)$ is not indicated.

Upon using the evolution laws (20) and (26), the free energy rate $\dot{\psi}_\mu$ can be expressed as

$$\dot{\psi}_\mu(\dot{\mathfrak{h}}) = \mathbf{P} \cdot \dot{\mathbf{F}} - (1-\eta)\sum_{s=1}^{n_s}\left(\tau_m^s\dot{\gamma}_m^s + q|\dot{\gamma}_m^s|\right) - \eta\sum_{s=1}^{n_s}\left(\tau_p^s\dot{\gamma}_p^s + q|\dot{\gamma}_p^s|\right) - (\tau_{\text{tw}}^* + f_\eta)\dot{\eta} - f_\chi\dot{\chi} - \mathbf{f}_{\nabla\chi}\cdot\nabla\dot{\chi}, \tag{37}$$

where the thermodynamic driving forces conjugate to $\bar{\gamma}$, η, χ and $\nabla\chi$ are expressed, respectively, as

$$q = -\frac{\partial\psi_\mu}{\partial\bar{\gamma}}, \qquad f_\eta = -\frac{\partial\psi_\mu}{\partial\eta}, \qquad f_\chi = -\frac{\partial\psi_\mu}{\partial\chi}, \qquad \mathbf{f}_{\nabla\chi} = -\frac{\partial\psi_\mu}{\partial\nabla\chi}, \tag{38}$$

and the resolved shear stresses τ_m^s and τ_p^s,

$$\tau_m^s = \mathbf{M}\cdot(\mathbf{s}_m^s \otimes \mathbf{n}_m^s), \qquad \tau_p^s = \mathbf{M}\cdot(\mathbf{s}_p^s \otimes \mathbf{n}_p^s), \tag{39}$$

are defined in terms of the Mandel stress $\mathbf{M}$, in agreement with the classical finite-strain crystal plasticity theory (Hill and Rice, 1972; Asaro, 1983). Finally, the stress-induced driving force for twinning has the following form,

$$\tau_{\text{tw}}^* = \mathbf{M}\cdot\log\mathbf{U}_{\text{tw}}, \tag{40}$$

that results from the kinematic assumption in Eq. (20), and $\tau_{\text{tw}}^* + f_\eta$ is the total driving force for twinning. Considering that $\log\mathbf{U}_{\text{tw}}$ is traceless, the driving force τ_{tw}^* is pressure insensitive, as expected. The star in the superscript is introduced to distinguish τ_{tw}^*, which depends on the magnitude of twinning deformation, from the resolved shear stresses τ_m^s and τ_p^s.

In order to arrive at a global variational formulation of the model, let us introduce the functional of the total potential energy, $\mathcal{E} = \Psi + \Omega$, where $\Psi = \int_B \psi_\mu \mathrm{d}V$ is the total free energy and Ω is the potential of external loads (assumed conservative), which is left unspecified. The rate of the potential energy takes thus the following form,

$$\dot{\mathcal{E}}[\dot{\boldsymbol{\varphi}}, \dot{\boldsymbol{\gamma}}, \dot{\eta}, \dot{\chi}] = \dot{\Psi}[\dot{\boldsymbol{\varphi}}, \dot{\boldsymbol{\gamma}}, \dot{\eta}, \dot{\chi}] + \dot{\Omega}[\dot{\boldsymbol{\varphi}}], \qquad \dot{\Psi}[\dot{\boldsymbol{\varphi}}, \dot{\boldsymbol{\gamma}}, \dot{\eta}, \dot{\chi}] = \int_B \dot{\psi}_\mu(\dot{\mathfrak{h}})\mathrm{d}V, \tag{41}$$

where B denotes the domain occupied by the body in the reference configuration. In the present notation, the arguments of the functions are placed inside round brackets, while the arguments of the functionals, i.e., the functions, are placed inside square brackets. Next, the global rate-potential is defined,

$$\Pi[\dot{\boldsymbol{\varphi}}, \dot{\boldsymbol{\gamma}}, \dot{\eta}, \dot{\chi}] = \dot{\mathcal{E}}[\dot{\boldsymbol{\varphi}}, \dot{\boldsymbol{\gamma}}, \dot{\eta}, \dot{\chi}] + \mathcal{D}[\dot{\boldsymbol{\gamma}}, \dot{\eta}], \qquad \mathcal{D}[\dot{\boldsymbol{\gamma}}, \dot{\eta}] = \int_B D(\dot{\boldsymbol{\gamma}}, \dot{\eta})\mathrm{d}V, \tag{42}$$

where D is the local dissipation potential that contains contributions from plastic slip (within the matrix and the twin) and twinning,

$$D(\dot{\boldsymbol{\gamma}}, \dot{\eta}) = D_m(\dot{\boldsymbol{\gamma}}_m) + D_p(\dot{\boldsymbol{\gamma}}_p) + D_{\text{tw}}(\dot{\eta}). \tag{43}$$

Each dissipation contribution in Eq. (43) consists of rate-independent and viscous parts. The plastic slip contributions, D_m and D_p, are defined as

$$D_m(\dot{\boldsymbol{\gamma}}_m) = (1-\eta)\sum_{s=1}^{n_s}\tau_m^{c,s}\left(|\dot{\gamma}_m^s| + \frac{(\dot{\gamma}_m^s)^2}{2\dot{\gamma}_0}\right), \qquad D_p(\dot{\boldsymbol{\gamma}}_p) = \eta\sum_{s=1}^{n_s}\tau_p^{c,s}\left(|\dot{\gamma}_p^s| + \frac{(\dot{\gamma}_p^s)^2}{2\dot{\gamma}_0}\right), \tag{44}$$

where $\tau_m^{c,s}$ and $\tau_p^{c,s}$ denote the critical resolved shear stresses of individual slip systems, respectively, in the matrix and in the twin, and characterize the respective rate-independent thresholds for the plastic slip. The viscous (rate-dependent) contribution is additionally characterized by the reference slip rate $\dot{\gamma}_0$. Note that here, for simplicity, an identical reference slip rate $\dot{\gamma}_0$ is assumed for all the slip systems in the matrix and in the twin, while in a more general setting, $\dot{\gamma}_0$ may vary from one slip system to another.

The twinning contribution to dissipation, D_{tw}, is specified by postulating the following form of the dissipation potential expressed in terms of v_n, the propagation speed of a smooth sharp twin interface (in the direction normal to the interface),

$$\hat{D}_{\text{tw}}(v_n) = \tau_{\text{tw}}^c\gamma_{\text{tw}}\left(|v_n| + \frac{v_n^2}{2v_0}\right), \tag{45}$$

where τ_{tw}^c is the critical resolved shear stress for twinning, and v_0 is the reference interface propagation speed. We refer here to the general notion of a sharp interface, assumed smooth at the scale of interest, and $\hat{D}_{\text{tw}}$ is the density per unit area of the interface in the reference configuration. Considering the theoretical profile of the order parameter η across a propagating diffuse interface, the dissipation potential $\hat{D}_{\text{tw}}(v_n)$ can be equivalently formulated in terms of $\dot{\eta}$ (Tůma et al., 2018),

$$D_{\text{tw}}(\dot{\eta}) = \tau_{\text{tw}}^c\gamma_{\text{tw}}\left(|\dot{\eta}| + \frac{\dot{\eta}^2}{2\dot{\eta}_0}\right), \qquad \dot{\eta}_0 = \frac{\pi v_0}{8\ell}, \tag{46}$$

where the reference rate $\dot{\eta}_0$ depends on the reference interface propagation speed v_0 and on ℓ, the interface thickness parameter, see Eqs. (30) and (31). Associated with a diffuse interface, D_{tw} is the density per unit volume in the reference configuration such that the integral of D_{tw} over the interface thickness is equal to $\hat{D}_{\text{tw}}$.

The complete evolution problem is now formulated as the following global minimization problem (Hildebrand and Miehe, 2012; Tůma et al., 2016, 2018),

$$\{\dot{\boldsymbol{\varphi}}, \dot{\boldsymbol{\gamma}}, \dot{\eta}, \dot{\chi}\} = \arg \min_{\dot{\boldsymbol{\varphi}}, \dot{\boldsymbol{\gamma}}, \dot{\eta}, \dot{\chi}} \Pi[\dot{\boldsymbol{\varphi}}, \dot{\boldsymbol{\gamma}}, \dot{\eta}, \dot{\chi}]. \tag{47}$$

It is shown in Section 3.3 that the necessary conditions for the minimum of the rate-potential Π deliver the governing equations of the evolution problem.

Since the free energy function ψ_μ and the dissipation potential D do not depend on the gradients of $\dot{\boldsymbol{\gamma}}$ and $\dot{\eta}$ (the gradient of $\dot{\eta}$ is not involved thanks to the micromorphic formulation), the minimization of Π with respect to $\dot{\boldsymbol{\gamma}}$ and $\dot{\eta}$ can be performed locally at each material point. The local minimization problem is therefore formulated in the following form

$$\{\dot{\boldsymbol{\gamma}}, \dot{\eta}\} = \arg \min_{\dot{\boldsymbol{\gamma}}, \dot{\eta}} \pi(\dot{\mathbf{F}}, \dot{\boldsymbol{\gamma}}, \dot{\eta}, \dot{\chi}, \nabla \dot{\chi}), \tag{48}$$

where π is the local rate-potential,

$$\pi(\dot{\mathbf{F}}, \dot{\boldsymbol{\gamma}}, \dot{\eta}, \dot{\chi}, \nabla \dot{\chi}) = \dot{\psi}_\mu(\dot{\mathbf{F}}, \dot{\boldsymbol{\gamma}}, \dot{\eta}, \dot{\chi}, \nabla \dot{\chi}) + D(\dot{\boldsymbol{\gamma}}, \dot{\eta}). \tag{49}$$

Accordingly, the reduced local potential π^{red} can be introduced,

$$\pi^{\text{red}}(\dot{\mathbf{F}}, \dot{\chi}, \nabla \dot{\chi}) = \min_{\dot{\boldsymbol{\gamma}}, \dot{\eta}} \pi(\dot{\mathbf{F}}, \dot{\boldsymbol{\gamma}}, \dot{\eta}, \dot{\chi}, \nabla \dot{\chi}), \tag{50}$$

and thereby the global variables $\dot{\boldsymbol{\varphi}}$ and $\dot{\chi}$ are determined by minimizing the global reduced potential Π^{red},

$$\{\dot{\boldsymbol{\varphi}}, \dot{\chi}\} = \arg \min_{\dot{\boldsymbol{\varphi}}, \dot{\chi}} \Pi^{\text{red}}[\dot{\boldsymbol{\varphi}}, \dot{\chi}], \qquad \Pi^{\text{red}}[\dot{\boldsymbol{\varphi}}, \dot{\chi}] = \int_B \pi^{\text{red}}(\nabla \dot{\boldsymbol{\varphi}}, \dot{\chi}, \nabla \dot{\chi}) \mathrm{d}V + \dot{\Omega}[\dot{\boldsymbol{\varphi}}]. \tag{51}$$

3.3. Governing equations in explicit form

The local rate-potential π is a convex function of $\dot{\boldsymbol{\gamma}}$ and $\dot{\eta}$, and it is non-smooth in view of the contributions of the rate-independent dissipation, cf. Eqs. (44) and (46), and of the accumulated plastic slip $\bar{\gamma}$, cf. Eqs. (26) and (37). The necessary and sufficient conditions for the minimum of π with respect to $\dot{\boldsymbol{\gamma}}$ and $\dot{\eta}$ take thus the form of the following inclusions,

$$\mathbf{0} \in \partial_{\dot{\boldsymbol{\gamma}}} \pi(\dot{\mathfrak{h}}), \qquad 0 \in \partial_{\dot{\eta}} \pi(\dot{\mathfrak{h}}), \tag{52}$$

where $\partial_{\dot{\boldsymbol{\gamma}}} \pi$ and $\partial_{\dot{\eta}} \pi$ denote the subdifferentials of π (Rockafellar, 1970). To prove the convexity of $\pi = \dot{\psi}_\mu + D$ with respect to $\dot{\boldsymbol{\gamma}}$ and $\dot{\eta}$ we note that $\dot{\psi}_\mu$ is a convex function of $\dot{\gamma}_{\text{m}}^s$ and $\dot{\gamma}_{\text{p}}^s$ (since $-q = H\bar{\gamma} \geq 0$ and $0 \leq \eta \leq 1$) and it is linear in $\dot{\eta}$, see Eq. (37), while D is obviously convex.

Inclusion (52)$_1$ yields the evolution equation for the slip rates,

$$\dot{\gamma}_k^s = \dot{\gamma}_0 \, \mathrm{sign}(\tau_k^s) \frac{\langle |\tau_k^s| - (\tau_k^{\text{c},s} + H\bar{\gamma}) \rangle}{\tau_k^{\text{c},s}}, \qquad k \in \{\text{m}, \text{p}\}, \tag{53}$$

where the Macaulay bracket $\langle x \rangle = \frac{1}{2}(|x| + x)$ returns x if x is positive, and zero otherwise. Note that the identity $\mathrm{sign}(\dot{\gamma}_k^s) = \mathrm{sign}(\tau_k^s)$ has been taken into account in Eq. (53). It follows that the dissipation potentials D_{m} and D_{p}, Eq. (44), and likewise D_{tw} in Eq. (46), define a Perzyna-type flow rule with a rate-independent threshold and plastic slip proportional to the overstress.

Similarly, the evolution law for the order parameter η can be derived from the inclusion (52)$_2$ in the following form,

$$\dot{\eta} = \dot{\eta}_0 \, \mathrm{sign}(\tau_{\text{tw}}^* + f_\eta) \frac{\langle |\tau_{\text{tw}}^* + f_\eta| - \tau_{\text{tw}}^{\text{c}} \gamma_{\text{tw}} \rangle}{\tau_{\text{tw}}^{\text{c}} \gamma_{\text{tw}}}, \tag{54}$$

where

$$f_\eta = -\frac{\partial \psi_\mu}{\partial \eta} = -\frac{1}{2} \mathbf{H}_{\text{e}} \cdot (\mathbb{L}_{\text{p}} - \mathbb{L}_{\text{m}}) \mathbf{H}_{\text{e}} - \Delta f(1 - 2\eta) - \epsilon_\mu(\eta - \chi) - \lambda, \tag{55}$$

$\lambda = \partial I_{[0,1]}^\epsilon / \partial \eta$, and it can be shown that $\mathrm{sign}(\dot{\eta}) = \mathrm{sign}(\tau_{\text{tw}}^* + f_\eta)$.

On the other hand, the condition of stationarity of the global potential Π^{red}, Eq. (51), with respect to $\dot{\boldsymbol{\varphi}}$,

$$0 = \delta_{\dot{\boldsymbol{\varphi}}} \Pi^{\text{red}}[\dot{\boldsymbol{\varphi}}, \dot{\chi}] = \int_B \mathbf{P} \cdot \nabla \delta \dot{\boldsymbol{\varphi}} \, \mathrm{d}V - \int_{\partial B_t} \mathbf{t}^* \cdot \delta \dot{\boldsymbol{\varphi}} \mathrm{d}S \qquad \forall \delta \dot{\boldsymbol{\varphi}}, \tag{56}$$

delivers the mechanical equilibrium equation in weak form, where $\delta \dot{\boldsymbol{\varphi}}$ denotes the kinematically admissible variation of $\dot{\boldsymbol{\varphi}}$. To fix attention, the potential of the external loads in Eq. (56) has been assumed as $\Omega = -\int_B \mathbf{t}^* \cdot \dot{\boldsymbol{\varphi}}$, where $\mathbf{t}^*$ denotes the nominal traction prescribed over the boundary ∂B_t. Note that the stationarity condition $\delta_{\dot{\boldsymbol{\varphi}}} \Pi^{\text{red}} = 0$ imposes the equilibrium condition on $\boldsymbol{\varphi}$ rather than on $\dot{\boldsymbol{\varphi}}$ since Π^{red} is a linear functional of $\dot{\boldsymbol{\varphi}}$ (Tůma et al., 2016).

Finally, stationarity of Π^{red} with respect to $\dot{\chi}$ is expressed as

$$0 = \delta_{\dot{\chi}} \Pi^{\text{red}}[\dot{\boldsymbol{\varphi}}, \dot{\chi}] = \int_B \left(\epsilon_\mu(\chi - \eta)\delta\dot{\chi} + \kappa \nabla \chi \cdot \nabla \delta \dot{\chi} \right) \mathrm{d}V \qquad \forall \delta \dot{\chi}, \tag{57}$$

where $\delta\dot{\chi}$ denotes an admissible variation of $\dot{\chi}$. Eq. (57) is, in fact, a weak form of the following Helmholtz-type PDE,

$$\chi - \ell_\mu \nabla^2 \chi = \eta, \qquad \ell_\mu = \sqrt{\frac{\kappa}{\epsilon_\mu}}, \tag{58}$$

which emerges in a natural way as a result of the micromorphic regularization with ℓ_μ as the corresponding characteristic length-scale (Forest, 2009).

The above PDE can be accompanied by the usual boundary conditions that replace the corresponding boundary conditions on the order parameter in a conventional (non-micromorphic) phase-field model. If a Dirichlet boundary condition, $\chi = \chi^*$, or a homogeneous Neumann boundary condition, $\nabla\chi \cdot \mathbf{n} = 0$, or a periodic boundary condition is adopted on ∂B, then the related boundary contribution to the total potential energy $\mathcal{E}$ vanishes, as assumed in this paper, see Eq. (41). In the case of periodic and homogeneous Neumann boundary conditions, one can show that $\int_B \chi\, dV = \int_B \eta\, dV$ so that χ approximates η not only locally (through the penalty term ψ_{pen}), but also globally. Periodic boundary conditions (on the boundary of the computational domain) and homogeneous Neumann boundary conditions (on the grain boundaries) are used in the examples studied in Section 5.

Remark 3.1. It is stressed that the present model does not require any special treatment of twin nucleation. This is because the order parameter η is directly used in the logarithmic mixing rule, Eq. (19), rather than through a nonlinear (typically polynomial) interpolation function. Accordingly, for $\eta = 0$ (and for $\eta = 1$), the evolution of η is triggered once the transformation condition, $|\tau_{\text{tw}}^* + f_\eta| - \tau_{\text{tw}}^c \gamma_{\text{tw}} > 0$, is satisfied, see Eq. (54). This feature is distinct from the usual phase-field formulations (e.g., Clayton and Knap, 2011; Liu et al., 2018a,b; Hu et al., 2021; Ma and Sun, 2021) that employ a nonlinear interpolation function, the derivative of which vanishes for $\eta = 0$ and 1, and, as a result, the driving force for twinning vanishes at these points. This necessitates a special treatment to trigger nucleation, such as a stochastic twin nucleation model applied at grain boundaries (Liu et al., 2018b), Langevin noise (Liu et al., 2018a), or introduction of local random fluctuations of the order parameter (Hu et al., 2021). Clearly, if the initial state is homogeneous, or piecewise homogeneous, as in the examples studied in Sections 5.2–5.4, the present model would predict a homogeneous evolution of η in the entire domain. A twin nucleus is then introduced to trigger localized twinning, which is a common practice in such idealized problems. However, no twin nucleus is introduced in the 10-grain problem in Section 5.5. Likewise, twin transmission in the bi-crystal problem of Section 5.4 is triggered solely by the local stress inhomogeneity caused by the primary twin impinging at the grain boundary.

3.4. Time-integration scheme

The rate evolution problem described above is now discretized in time by using the backward Euler scheme. We denote the current time instant by t_{n+1} and the previous time instant by t_n, where $t_{n+1} = t_n + \Delta t$. The corresponding variables are thereby labeled by the superscripts $n+1$ and n, respectively, with the latter considered to be known. The incremental form of the evolution law (20) is obtained by applying the volume-preserving exponential mapping (e.g. Miehe, 1996),

$$\mathbf{F}_{\text{in}}^{n+1} = \exp(\Delta t\, \mathbf{L}_{\text{in}}^{n+1})\mathbf{F}_{\text{in}}^n, \tag{59}$$

where

$$\Delta t\, \mathbf{L}_{\text{in}}^{n+1} = (1-\eta)\sum_{s=1}^{n_s} \Delta\gamma_{\text{m}}^s \mathbf{s}_{\text{m}}^s \otimes \mathbf{n}_{\text{m}}^s + \eta\sum_{s=1}^{n_s} \Delta\gamma_{\text{p}}^s \mathbf{s}_{\text{p}}^s \otimes \mathbf{n}_{\text{p}}^s + \Delta\eta \log(\mathbf{U}_{\text{tw}}), \tag{60}$$

and $\Delta\gamma_{\text{m}}^s$, $\Delta\gamma_{\text{p}}^s$ and $\Delta\eta$ are the increments of the respective quantities.

We begin the formulation of the incremental minimization problem by rewriting the local minimization rate-problem, Eq. (48), such that the state-dependence on the order parameter η is indicated explicitly (the reason for this treatment is explained later),

$$\{\dot{\gamma},\dot{\eta}\} = \arg\min_{\dot{\gamma},\dot{\eta}} \pi(\dot{\mathbf{F}},\dot{\gamma},\dot{\eta},\dot{\chi},\nabla\dot{\chi};\eta), \tag{61}$$

where π is here rewritten as

$$\pi(\dot{\mathbf{F}},\dot{\gamma},\dot{\eta},\dot{\chi},\nabla\dot{\chi};\eta) = \dot{\psi}_\mu(\dot{\mathbf{F}},\dot{\gamma},\dot{\eta},\dot{\chi},\nabla\dot{\chi};\eta) + D(\dot{\gamma},\dot{\eta};\eta). \tag{62}$$

At the current time instant t_{n+1}, the local rate potential π in Eq. (62) is approximated by using the backward Euler scheme. In order to make the notation more concise and consistent with the rate formulation in Section 3.2, a new vector $\Delta\mathfrak{h}$ is defined,

$$\Delta\mathfrak{h} = \{\mathbf{F}^{n+1}, \Delta\boldsymbol{\gamma}, \Delta\eta, \Delta\chi, \nabla(\Delta\chi)\}, \tag{63}$$

where $\Delta\boldsymbol{\gamma} = \{\Delta\boldsymbol{\gamma}_{\text{m}}, \Delta\boldsymbol{\gamma}_{\text{p}}\}$. Note that the symbol $\Delta\mathfrak{h}$ (notice the Δ) has been exploited here since it collects all the quantities related to the incremental formulation, while it does not merely represent the increments of all related quantities. Note also that $\mathbf{F}_{\text{in}}^{n+1}$ does not appear here as an independent variable, as it is explicitly defined by Eqs. (59)–(60).

The rate-potential π is now approximated as

$$\pi(\dot{\mathfrak{h}};\eta)\Big|_{t=t_{n+1}} \approx \frac{1}{\Delta t}\Delta\pi(\Delta\mathfrak{h};\tilde{\eta}^{n+1}), \tag{64}$$

where the incremental potential $\Delta\pi$ is defined as

$$\Delta\pi(\Delta\mathfrak{h};\tilde{\eta}^{n+1}) = \psi_\mu^{n+1}(\Delta\mathfrak{h};\tilde{\eta}^{n+1}) - \psi_\mu^n + \Delta D(\Delta\boldsymbol{\gamma},\Delta\eta;\tilde{\eta}^{n+1}), \tag{65}$$

ψ_μ^{n+1} denotes the free energy at t_{n+1} that is evaluated according to Eq. (32),

$$\psi_\mu^{n+1}(\Delta\mathfrak{h};\tilde{\eta}^{n+1}) = \psi_\mu(\mathbf{F}^{n+1}, \mathbf{F}_{\text{in}}^{n+1}, \bar{\gamma}^{n+1}, \eta^{n+1}, \chi^{n+1}, \nabla\chi^{n+1}), \tag{66}$$

and the accumulated plastic slip at t_{n+1} is integrated as, cf. Eq. (26),

$$\bar{\gamma}^{n+1} = \bar{\gamma}^n + (1 - \tilde{\eta}^{n+1}) \sum_{s=1}^{n_s} |\Delta\gamma_{\text{m}}^s| + \tilde{\eta}^{n+1} \sum_{s=1}^{n_s} |\Delta\gamma_{\text{p}}^s|. \tag{67}$$

Note that an independent variable $\tilde{\eta}^{n+1}$ has been introduced above to distinguish the dependence of $\Delta\pi$ on the current value of $\eta = \tilde{\eta}^{n+1}$ that results from the state-dependence of π on η, as indicated in Eq. (62), from the dependence of $\Delta\pi$ on the current value of $\eta = \eta^{n+1} = \eta^n + \Delta\eta$ that results from the dependence of π on $\dot{\eta}$. This distinction is important to preserve the consistency of the incremental minimization problem introduced below, Eq. (72), with the original rate problem (61).

Upon applying the backward Euler scheme, the time-discrete dissipation potential $\Delta D \approx \Delta t D$ is obtained as,

$$\Delta D(\Delta\boldsymbol{\gamma}, \Delta\eta; \tilde{\eta}^{n+1}) = \Delta D_{\text{m}}(\Delta\boldsymbol{\gamma}_{\text{m}}; \tilde{\eta}^{n+1}) + \Delta D_{\text{p}}(\Delta\boldsymbol{\gamma}_{\text{p}}; \tilde{\eta}^{n+1}) + \Delta D_{\text{tw}}(\Delta\eta), \tag{68}$$

where the time-discrete dissipation contributions resulting from the respective rate forms, Eqs. (44) and (46), are expressed as

$$\Delta D_{\text{m}}(\Delta\boldsymbol{\gamma}_{\text{m}}; \tilde{\eta}^{n+1}) = (1 - \tilde{\eta}^{n+1}) \sum_{s=1}^{n_s} \tau_{\text{m}}^{\text{c},s} \left(|\Delta\gamma_{\text{m}}^s| + \frac{(\Delta\gamma_{\text{m}}^s)^2}{2\Delta t \dot{\gamma}_0} \right), \tag{69}$$

$$\Delta D_{\text{p}}(\Delta\boldsymbol{\gamma}_{\text{p}}; \tilde{\eta}^{n+1}) = \tilde{\eta}^{n+1} \sum_{s=1}^{n_s} \tau_{\text{p}}^{\text{c},s} \left(|\Delta\gamma_{\text{p}}^s| + \frac{(\Delta\gamma_{\text{p}}^s)^2}{2\Delta t \dot{\gamma}_0} \right), \tag{70}$$

and

$$\Delta D_{\text{tw}}(\Delta\eta) = \tau_{\text{tw}}^{\text{c}} \gamma_{\text{tw}} \left(|\Delta\eta| + \frac{\Delta\eta^2}{2\Delta t \dot{\eta}_0} \right). \tag{71}$$

Finally, the local incremental minimization problem is formulated as

$$\{\Delta\boldsymbol{\gamma}, \Delta\eta\} = \arg\min_{\Delta\boldsymbol{\gamma}, \Delta\eta} \Delta\pi(\mathbf{F}^{n+1}, \Delta\boldsymbol{\gamma}, \Delta\eta, \Delta\chi, \nabla(\Delta\chi); \tilde{\eta}^{n+1}). \tag{72}$$

It is stressed that the minimization problem (72) is not a standard optimization problem but rather a *quasi*-optimization problem.[1] In the rate-problem (48), minimization is performed with respect to $\dot{\eta}$ at fixed η. In a consistent manner, minimization in Eq. (72) is performed with respect to $\Delta\eta$, but not with respect to $\tilde{\eta}^{n+1}$ which, however, coincides with η^{n+1} and thus depends on $\Delta\eta$, but the substitution $\tilde{\eta}^{n+1} = \eta^{n+1}$ is to be made after establishing the necessary condition for the minimum of $\Delta\pi$ with respect to $\Delta\eta$. In analogy to the inclusions in Eq. (52), the time-discrete evolution equations for $\Delta\boldsymbol{\gamma}$ and $\Delta\eta$ result from the following inclusions,

$$\mathbf{0} \in \partial_{\Delta\boldsymbol{\gamma}} \Delta\pi(\Delta\mathfrak{h}, \tilde{\eta}^{n+1}), \qquad 0 \in \partial_{\Delta\eta} \Delta\pi(\Delta\mathfrak{h}, \tilde{\eta}^{n+1}). \tag{73}$$

Note that the incremental potential $\Delta\pi$ is in general not convex in $\Delta\eta$, but it is convex if Δt is sufficiently small (Tůma et al., 2018, Appendix B), and the inclusion in Eq. (73)$_2$ is to be understood in this sense. In practice, we have not encountered any problems related to non-convexity of $\Delta\pi$.

The rest of the procedure follows that of the rate-problem presented in Section 3.2. Specifically, a global incremental potential is defined and is minimized with respect to the global fields ($\boldsymbol{\varphi}^{n+1}$, χ^{n+1}), see Section 3.3.

4. Finite-element implementation

In this work, the finite-element method is employed for the spatial discretization of the governing equations. The problem at hand comprises two global unknown fields, namely the displacement $\mathbf{u} = \boldsymbol{\varphi} - \mathbf{X}$ and the micromorphic variable χ. The computations are limited to 2D plane-strain problems, see Section 5. Accordingly, the 8-noded elements with serendipity shape functions (with the reduced 2×2 Gauss quadrature rule) are used to discretize the displacement field $\mathbf{u}$, while the 4-noded elements with bi-linear shape functions (with the standard 2×2 Gauss quadrature rule) are used for the micromorphic variable χ. Based on the results of our supplementary analyses and also our prior modeling experiences in other contexts, this discretization scheme leads to more efficient computations and more accurate results compared to other possibilities tested.

The local sub-problem, Eq. (72), is a non-smooth minimization problem to be solved at each Gauss point. The non-smoothness, which requires adequate handling in the finite-element implementation, arises from the rate-independent dissipation contributions, Eqs. (69)–(71), from the inequality constraints on the twinning order parameter, Eq. (27), and from the absolute value function in the definition of the accumulated plastic slip, Eq. (67). Following Stupkiewicz and Petryk (2013), the augmented Lagrangian

---

[1] The quasi-optimization problem (72) can be formally written in the following form,

$$\{\Delta\boldsymbol{\gamma}^*, \Delta\eta^*\} = \arg\min_{\Delta\boldsymbol{\gamma}, \Delta\eta} \Delta\pi(\mathbf{F}^{n+1}, \Delta\boldsymbol{\gamma}, \Delta\eta, \Delta\chi, \nabla(\Delta\chi); \eta^n + \Delta\eta^*),$$

with $(\Delta\boldsymbol{\gamma}^*, \Delta\eta^*)$ denoting the solution of the problem. Similar quasi-optimization problems emerge, for instance, in frictional contact problems (Alart and Curnier, 1991), see also Petryk (2020).
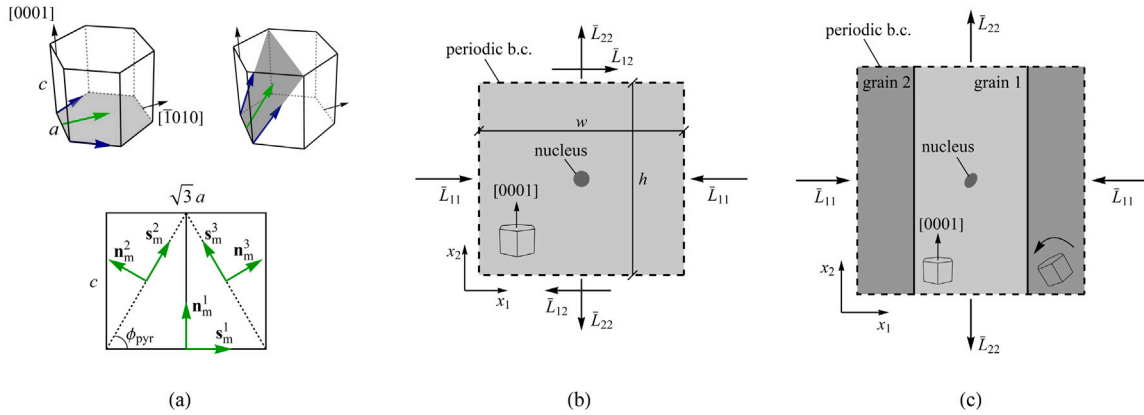
Fig. 4. The setup of illustrative 2D problems: (a) the operative slip systems considered; (b) sketch of problem #1 and #2; (c) sketch of problem #3.

method is exploited here to replace the non-smooth minimization problem by an equivalent smooth saddle-point problem. The corresponding Lagrange function is defined in terms of the primal unknowns ($\Delta\gamma = \{\Delta\gamma_{\mathrm{m}}, \Delta\gamma_{\mathrm{p}}\}$ and $\Delta\eta$) and the respective Lagrange multipliers. As the Lagrange function is continuously differentiable, the necessary condition for the saddle point is solved using the Newton method. The details are omitted here.

The global system of equations resulting from the finite-element discretization is solved by means of the Newton method in a monolithic scheme. Computer implementation has been done in *AceGen* (Korelc and Wriggers, 2016). *AceGen* is a code generation tool that delivers automatic differentiation (AD) and advanced code simplification techniques. As a consequence, the derived finite-element codes are highly efficient, and most importantly, an exact tangent matrix is achieved, which is essential to obtain an optimum convergence of the Newton method. A closed-form representation of the matrix exponential and matrix logarithm is available in *AceGen* (Korelc and Stupkiewicz, 2014; Hudobivnik and Korelc, 2016), which facilitates direct implementation of the exponential mapping, Eq. (60), and the matrix logarithm in the logarithmic elastic strain, Eq. (28), including the respective first and second derivatives.

Finite-element computations are done in *AceFEM*, a finite-element environment that is closely integrated with *AceGen*. A direct linear solver (MKL PARDISO) is employed to solve the linear system at each iteration of the Newton method. All the computations were conducted on a 12-core workstation equipped with an Intel i9-10920X CPU and 128 GB RAM.

5. Illustrative examples

In this section, four representative 2D plane-strain problems are studied to illustrate the features and capabilities of the proposed model. The first study is aimed at illustrating the impact of the adopted kinematics of deformation twinning. The second and third studies are intended to address, respectively, the twin evolution in a single crystal under combined tension–shear loading, and the twin transmission across grain boundaries in a bi-crystal setup. In the final study, the nucleation and evolution of twins and the interaction of twinning and plastic slip is investigated in a unit cell containing 10 grains.

5.1. Problem setup

In the numerical examples reported below, we assume that only one twin deformation variant, and thus only two conjugate twinning systems, can be active. Accordingly, we consider a class of 2D plane-strain problems in the $(\bar{1}2\bar{1}0)$ plane which admits such plane-strain deformation, see Fig. 1. To preserve plane-strain conditions, the slip systems must be adequately defined, as discussed below.

In general, HCP metals have 30 slip systems, out of which basal (3), prismatic (3) and second-order $\langle a+c \rangle$ pyramidal (6) slip systems are predominantly activated in magnesium according to the experimental observations, and thus must be considered in full 3D computations (Kelley and Hosford, 1968; Graff et al., 2007). In the present simplified 2D setting, we consider three equivalent in-plane slip systems that admit plane-strain deformation. First, an equivalent basal slip system with the (0001) slip plane and $[\bar{1}010]$ slip direction is considered that represents two (co-planar) crystallographic basal slip systems with the $[\bar{2}110]$ and $[\bar{1}\bar{1}20]$ slip directions, which are assumed to slip concurrently and by the same amount. Likewise, we consider two symmetric equivalent pyramidal slip systems with the $(10\bar{1}1)$ and $(\bar{1}011)$ slip planes, each representing two crystallographic co-planar $\langle a+c \rangle$ pyramidal slip systems. The operative slip systems (one basal and two pyramidal, numbered respectively 1 to 3) are shown in Fig. 4(a), where $\tan\phi_{\mathrm{pyr}} = 2c/(\sqrt{3}a)$ (and $\phi_{\mathrm{pyr}} = 61.9°$ for Mg).

The following material and model parameters are adopted in all computations, unless explicitly mentioned otherwise. The material parameters are typical for magnesium, which has the c/a ratio of 1.624 and thus a twinning shear angle of $\gamma_{\mathrm{tw}} = 0.129$ (Christian and Mahajan, 1995). The values of the critical resolved shear stresses (CRSS) for plastic slip and twinning in

magnesium have been the subject of considerable debate and research for many years. Studies indicate that the CRSS values of slip and twinning are influenced by many variables, including temperature, microstructural characteristics, deformation history, etc. (Akhtar and Teghtsoonian, 1969; Barnett et al., 2006; Al-Samman and Gottstein, 2008; Chapuis and Driver, 2011; Robson et al., 2013; Lynch et al., 2014; Wang et al., 2019; Liu et al., 2019; Li et al., 2021). It is often assumed that tensile twinning and basal slip systems have comparable CRSS values, although sometimes the CRSS for basal slip is assumed visibly lower than that for twinning. At the same time, the CRSS values for non-basal slip systems are usually larger by one order of magnitude. Accordingly, in the present simulations, a CRSS value of $\tau_{\mathrm{tw}}^{\mathrm{c}} = \tau_{\mathrm{m}}^{\mathrm{c},1} = \tau_{\mathrm{p}}^{\mathrm{c},1} = 15\,\mathrm{MPa}$ has been considered for tensile twinning and basal slip (in both matrix and twin), while a CRSS value of $\tau_{\mathrm{m}}^{\mathrm{c},i} = \tau_{\mathrm{p}}^{\mathrm{c},i} = 150\,\mathrm{MPa}$ ($i = 2, 3$) has been considered for the pyramidal slip systems (in both matrix and twin). The elastic constants c_{ij} of magnesium with an HCP crystal structure (having the transversely isotropic symmetry with five independent constants) are taken as $c_{11} = 63.5\,\mathrm{GPa}$, $c_{33} = 66.5\,\mathrm{GPa}$, $c_{12} = 25.9\,\mathrm{GPa}$, $c_{13} = 21.7\,\mathrm{GPa}$ and $c_{44} = 18.4\,\mathrm{GPa}$ (Slutsky and Garland, 1957). A hardening parameter of $H = 0.4\,\mathrm{GPa}$ and a reference plastic slip rate of $\dot{\gamma}_0 = 1\,\mathrm{s}^{-1}$ have been used. Moreover, a suitable reference twin interface propagation speed $v_0 = 100\,\mathrm{nm/s}$ has been adopted such that the viscous effects are not significant, i.e., the viscous overstress is of the order of maximum 10% of the rate-independent threshold (perhaps except at the twin tip which may propagate faster, but the related effects are localized and do not influence the overall response significantly). In general, both $\dot{\gamma}_0$ and v_0 have been selected such that the overall response is mostly governed by the rate-independent thresholds for slip and twinning and shows a weak rate-dependence for the loading rates used in the computations.

The parameters related to the twin-boundary energy and micromorphic regularization are specified next. The interfacial energy density $\Gamma = 0.15\,\mathrm{J/m}^2$ has been adopted, in line with the results of first-principles calculations and atomistic simulations (Wang et al., 2010a; Pei et al., 2017, 2018). This value is of the same order as those adopted in a number of phase-field studies of twinning in magnesium, e.g., $0.117\,\mathrm{J/m}^2$ (Clayton and Knap, 2011; Liu et al., 2018a) or $0.585\,\mathrm{J/m}^2$ (Ma and Sun, 2021). On the other hand, in some other studies, excessively large values of interfacial energy have been used, e.g., $2.95\,\mathrm{J/m}^2$ (Hu et al., 2021) or even $14\,\mathrm{J/m}^2$ (Liu et al., 2018b), as can be reckoned from the values of Δf and κ provided in these papers.

The interface thickness parameter of $\ell = 5\,\mathrm{nm}$ has been calibrated based on two criteria. Firstly, we note that the matrix–twin interfaces must be properly resolved by the finite-element mesh so that, in particular, an artificial increase of the twin-boundary energy is inhibited, see Levitas and Javanbakht (2011) and Tůma et al. (2021) for the related discussion. Accordingly, the value of ℓ sets an upper bound on the element size and, considering the overall computational cost, on the size of the computational domain, and thus ℓ must be possibly large. Secondly, an excessively large value of ℓ leads to unduly diffuse interfaces, and thereby spoils the spatial resolution and physical relevance of the simulated microstructure. Note that $\ell = 5\,\mathrm{nm}$ results in the theoretical interface thickness of $\pi\ell \approx 16\,\mathrm{nm}$ (in the direction normal to the interface and under stress-free conditions). With the above two parameters defined, the barrier and gradient energy coefficients are obtained as $\Delta f = 38\,\mathrm{MJ/m}^3$ and $\kappa = 0.95\,\mathrm{nJ/m}$, see Eq. (31). Finally, the micromorphic penalty parameter has been set to $\epsilon_\mu = 5\,\mathrm{GPa}$, which ensures a sufficiently small deviation between the local order parameter η and the global micromorphic variable χ at no significant extra computational cost, see Rezaee-Hajidehi and Stupkiewicz (2021) for a related study.

In all simulations, a rectangular computational domain is considered, which is discretized uniformly by a mesh of quadrilateral elements. Periodic boundary conditions are imposed, i.e., the displacement fluctuations and the micromorphic variable χ are assumed periodic in both horizontal and vertical directions (periodicity is enforced using Lagrange multipliers). A deformation-controlled loading is then applied by prescribing a constant macroscopic velocity gradient tensor $\bar{\mathbf{L}}$, which is defined in terms of a constant macroscopic (effective) strain rate $\bar{d}$ and a deviatoric tensor $\boldsymbol{\omega}$ that defines the loading path,

$$\bar{\mathbf{L}} = \frac{\sqrt{3}}{2}\bar{d}\boldsymbol{\omega}, \qquad \bar{d} = \sqrt{\frac{2}{3}\bar{\mathbf{D}} \cdot \bar{\mathbf{D}}}, \qquad \bar{\mathbf{D}} = \frac{1}{2}\left(\bar{\mathbf{L}} + \bar{\mathbf{L}}^{\mathrm{T}}\right). \tag{74}$$

Specifically, isochoric tension or combined isochoric tension–shear loading conditions are considered, thus the components of $\boldsymbol{\omega}$ are determined based on the loading angle ϕ_{L},

$$\boldsymbol{\omega} = \begin{pmatrix} -\cos\phi_{\mathrm{L}} & 2\sin\phi_{\mathrm{L}} \\ 0 & \cos\phi_{\mathrm{L}} \end{pmatrix}, \tag{75}$$

so that $\phi_{\mathrm{L}} = 0$ corresponds to tension along the x_2-direction and $\phi_{\mathrm{L}} = \pm 90°$ corresponds to simple shear.

5.2. Study #1: on the kinematics of deformation twinning

The objective of this study is to investigate the impact of the adopted kinematics of twinning on the evolution of the twin boundaries at the early stage of the matrix–twin transformation. Specifically, the performance of the logarithmic mixing rule (19) is compared to that of the rank-one mixing rule (21), see Remark 2.5. Since the main focus of this study is on the intrinsic evolution of the twin boundaries, plastic slip has been excluded.

A sketch of the problem setup is depicted in Fig. 4(b). The size of the simulation domain is $w \times h = 533 \times 500\,\mathrm{nm}^2$, with the width-to-height ratio of 1.07 as in the magnesium HCP unit cell ($\sqrt{3}a/c = 1.07$). The domain is discretized by the mesh with 42 600 elements (element size of 2.5 nm) leading to approximately 300 000 degrees of freedom. The initial lattice orientation of the matrix is set such that the local [0001]-axis is aligned with the global x_2-axis. A circular twin nucleus with the radius of 10 nm has been placed at the center of the simulation domain. An isochoric tension ($\phi_{\mathrm{L}} = 0$) along the x_2-axis is applied at a constant macroscopic strain rate of $\bar{d} = 0.1\,\mathrm{s}^{-1}$. In some cases, with the aim to break the symmetry and trigger a specific orientation of the twin, a small shear deformation (the overall shear strain of 0.02%) is applied prior to tension.
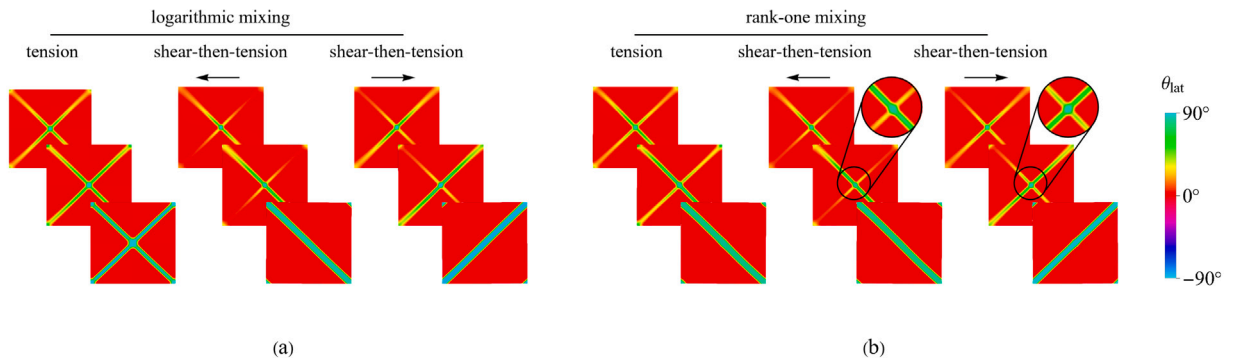
Fig. 5. The early-stage matrix–twin transformation predicted by models with different twinning kinematics: (a) logarithmic mixing rule (19), and (b) rank-one mixing rule (21). The arrows represent the direction of the initial shear in the case of combined shear-then-tension loading. The snapshots in each row belong to the same elongation.
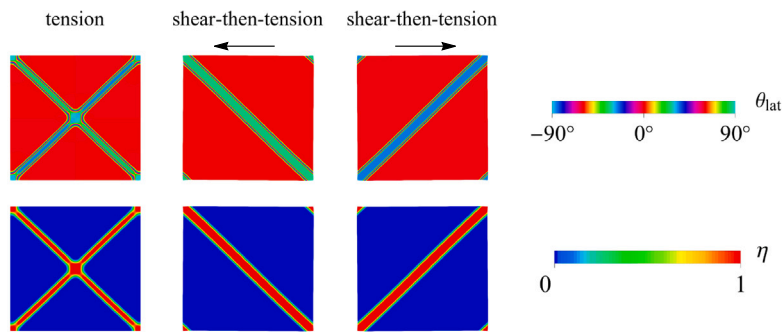

Fig. 6. Detailed view of the three microstructures from the bottom row in Fig. 5(a) represented here by a high-resolution color scale of the lattice orientation angle θ_{lat} (top) and by the order parameter η (bottom).

The snapshots of the early-stage matrix–twin transformation are shown in Fig. 5. The twin microstructure is represented by the spatial distribution of the lattice orientation angle θ_{lat} which is defined as the angle between the local [0001]-axis and the global x_2-axis, measured in the current configuration. The advantage of this representation compared to the typical distribution of the order parameter is that it brings more information. Indeed, lattice rotation is caused both by twinning and by plastic slip (present in the subsequent examples), hence activity of both mechanisms can be visualized using θ_{lat}. Moreover, lattice orientation changes gradually within the diffuse twin boundaries, hence the diffuseness of the interfaces is also visualized by θ_{lat}. To reflect the in-plane two-fold symmetry of the HCP unit cell (in 2D), a 180°-periodic color scale is used to depict θ_{lat}. The two representations are compared in Fig. 6, where the three microstructures from the bottom row in Fig. 5(a) are shown using the lattice orientation angle θ_{lat} (here represented by a color scale of a higher resolution) and using the order parameter η. Thanks to the higher resolution, the difference in the lattice orientation of the two conjugate twins is more apparent than in Fig. 5.

The results obtained for the logarithmic mixing rule are discussed first. Fig. 5(a), see also Fig. 6, shows that in the case with no initial shear applied (i.e., when the problem setup is symmetric), the twin nucleus develops into two symmetric crossing bands, comprising the two conjugate twins, one spanning from bottom-right to top-left (with the lattice orientation angle of $\theta_{\mathrm{lat}} = 86.3°$), and the other spanning from bottom-left to top-right (with the lattice orientation angle of $\theta_{\mathrm{lat}} = 93.7°$). This originates from the feature of the logarithmic mixing rule that treats the two conjugate twinning systems (corresponding to the two twin bands) equally. When the initial shear is applied, however, only one twin band develops, and its orientation is determined by the direction of this shear. Thanks to the symmetry of the formulation, the twin microstructure obtained for the initial shear directed to the left ($\phi_{\mathrm{L}} = -90°$) is perfectly the mirror image of that obtained for the initial shear directed to the right ($\phi_{\mathrm{L}} = 90°$). The lattice orientation angles of the two twin bands ($\theta_{\mathrm{lat}} = 86.3°$ and $93.7°$) agree perfectly with the theoretical orientation predicted by the sharp-interface theory discussed in Section 2.2 (note that the rotation tensors $\mathbf{R}_{\mathrm{tw}}^{(i)}$, cf. Fig. 1(c), correspond to a rotation by $\pm 3.7°$ so that the theoretical lattice orientation within the twin bands is indeed equal to $90° \pm 3.7°$).

In contrast to the logarithmic mixing rule, the model with the rank-one mixing rule has a propensity to develop a twin band with a specific orientation. This is obviously due to the fact that a specific conjugate twinning system is explicitly introduced into the kinematics within the diffuse interface. As shown in Fig. 5(b), a twin spanning from bottom-right to top-left ($\theta_{\mathrm{lat}} = 86.3°$) develops under isochoric tension with no initial shear, i.e., a non-symmetric solution is obtained even though the problem setup is symmetric. The propensity to develop this specific twin is also reflected in the case where the initial shear is applied. As it can be seen in the insets in Fig. 5(b), the early-stage evolution of the matrix–twin transformation in the case with the initial shear directed to the right
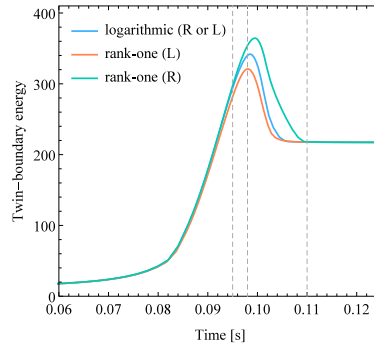
Fig. 7. Evolution of the twin-boundary energy $\Psi_\Gamma = \int_B \psi_\Gamma \mathrm{d}V$ at the early-stage of the matrix–twin transformation for the models with the logarithmic mixing rule and with the rank-one mixing rule. The letters in the parentheses denote the direction of the applied initial shear, 'R' and 'L' stand for right and left, respectively. The vertical dashed lines correspond to the time steps at which the snapshots in Fig. 5 are taken.

is visibly affected by the strong presence of this twin (i.e., at the intermediate stage shown in the insets, the top-right twin is much weaker in the case of the initial shear directed to the left than the top-left twin in the case of the initial shear directed to the right).

The above observations are quantitatively supported by the evolution of the total twin-boundary energy, $\Psi_\Gamma = \int_B \psi_\Gamma \mathrm{d}V$, cf. Eq. (30). Fig. 7 reveals that the model with the rank-one mixing rule predicts the highest peak energy (corresponding to the onset of the twin nucleus growth) for the initial shear directed to the right, which is about 1.15 times higher compared to the case of the initial shear directed to the left. At the same time, the peak energy evaluated for the model with the logarithmic mixing rule, regardless of the direction of the initial shear, lies between those obtained for the rank-one mixing rule. As the loading continues, the twin band spans the whole diagonal of the simulation domain, and the twin-boundary energy in all cases converges to the same value.

The above study confirms that, as expected, the logarithmic mixing rule preserves the symmetry of the twinning transformation and, unlike the rank-one mixing rule, treats both twinning systems equally, also in terms of the energy of diffuse interfaces, as discussed in Remark 2.5.

5.3. Study #2: single crystal under proportional tension–shear loading

In this study, as an essential preliminary step towards more realistic and complex scenarios, the interaction between plastic slip and twinning is investigated in an idealized single-crystal setup. To this end, the microstructure evolution and the associated mechanical response of the single crystal are studied under proportional combined isochoric tension–shear loading conditions. Only a single slip system, the basal slip, is considered in the matrix and in the twin. This simplification is reasonable and is in line with the experimental observations. Indeed, due to the high CRSS of non-basal slip systems with respect to that of the basal slip and tensile twinning, the contribution of the non-basal slip systems to the macroscopic deformation is not significant (Christian and Mahajan, 1995; Agnew et al., 2001, 2003; Barnett et al., 2006). This is also shown in the study of a 10-grain unit cell in Section 5.5.

The problem setup is depicted in Fig. 4(b), the model parameters are specified in Section 5.1, and the domain size and element size are the same as in the study #1 in Section 5.2. The combined loading is applied by varying the loading angle ϕ_L, see Eq. (75), between 0 (isochoric tension) and 90° (simple shear). A twin nucleus is placed at the center of the domain. The nucleus is now in the shape of an inclined ellipse whose major axis is parallel to the line extending from the lower-left to the upper-right corner of the simulation domain. The resulting twin bands have thus the same orientation for all loading angles ϕ_L, which simplifies the comparison of microstructure evolution. In order to keep the rate-dependent (viscoplastic) effects and the resulting overstress as low as possible, a relatively low macroscopic strain-rate of $\bar{d} = 0.01$ s^{-1} is used in this study.

The mechanical response of the single crystal under proportional loading is here expressed in terms of the macroscopic equivalent stress $\bar{\sigma}_{\mathrm{eq}}$ and strain $\bar{\varepsilon}_{\mathrm{eq}}$,

$$\bar{\sigma}_{\mathrm{eq}} = \sqrt{\frac{3}{2}\bar{\mathbf{S}} \cdot \bar{\mathbf{S}}}, \qquad \bar{\varepsilon}_{\mathrm{eq}} = \sqrt{\frac{2}{3}\bar{\mathbf{H}} \cdot \bar{\mathbf{H}}}, \tag{76}$$

where $\bar{\mathbf{S}}$ and $\bar{\mathbf{H}}$ denote, respectively, the macroscopic deviatoric Cauchy stress tensor and the macroscopic logarithmic strain tensor, $\bar{\mathbf{H}} = \frac{1}{2}\log(\bar{\mathbf{F}}^{\mathrm{T}}\bar{\mathbf{F}})$.

The results reveal that, except for the case of simple shear ($\phi_L = 90°$) where the twin nucleus does not grow at all, the overall appearance of the microstructure evolution is qualitatively similar for all loading angles ϕ_L. More specifically, the twin nucleus develops into a twin band spanning from bottom-left to top-right, and subsequently thickens in the transverse direction, until the entire simulation domain is transformed to the twin. A similar twin microstructure evolution has been reported in 3D analyses with non-basal slip systems involved (e.g., Liu et al., 2018b; Hu et al., 2021). As a representative illustration, the microstructure evolution and the deformation pattern are shown in Fig. 8 for $\phi_L = 22.5°$. The activity of plastic deformation is illustrated by the effective (accumulated) basal slip in the matrix, $\bar{\gamma}_{\mathrm{m}}$, and in the twin, $\bar{\gamma}_{\mathrm{p}}$, that are integrated according to Eq. (24). The main impact of the
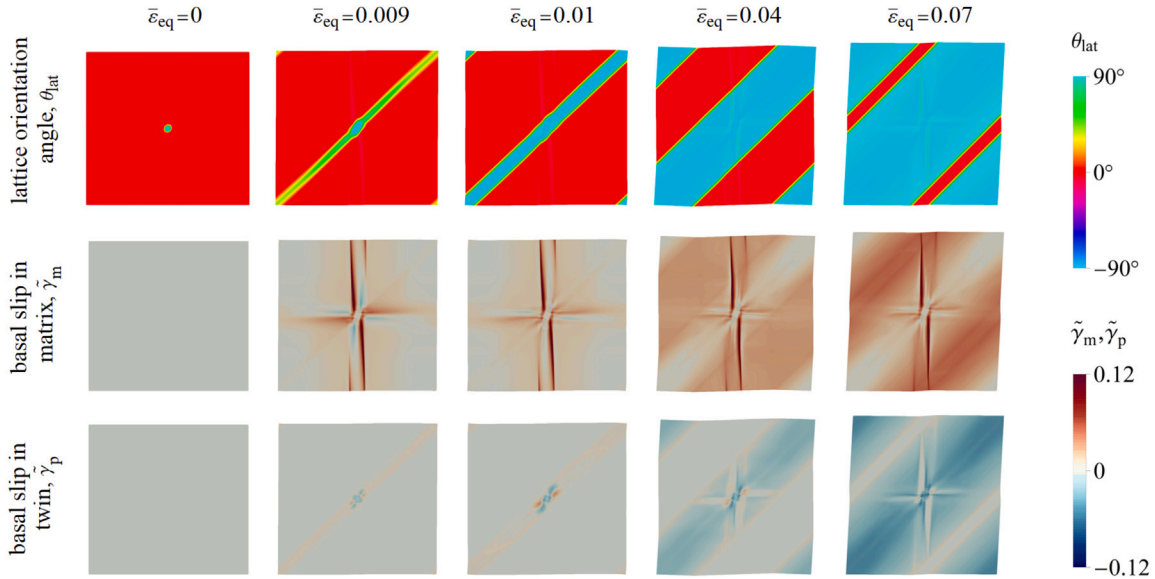
Fig. 8. Evolution of the lattice orientation angle θ_{lat} and effective basal slip in the matrix, $\tilde{\gamma}_{\mathrm{m}}$, and in the twin, $\tilde{\gamma}_{\mathrm{p}}$, for the loading angle $\phi_{\mathrm{L}} = 22.5°$.

loading angle ϕ_{L} pertains to the activity of the basal slip, which increases as ϕ_{L} increases, i.e., as the loading mode tends towards simple shear.

An eye-catching feature of the deformation pattern is the formation of vertical slip bands at the center of the simulation domain, see the snapshots of $\tilde{\gamma}_{\mathrm{m}}$ in Fig. 8. The vertical bands form at the initial stage of microstructure evolution (when the twin nucleus starts to grow), as a result of the stress concentration around the nucleus.

The effect of the loading angle ϕ_{L} on the macroscopic mechanical response is shown in Fig. 9(a). Except for the case of simple shear ($\phi_{\mathrm{L}} = 90°$), which exhibits a bilinear trend (elastic and plastic branches), the mechanical response involves several characteristic stages. The stage of stress overshoot and stress drop corresponds to twin propagation (i.e., growth of the nucleus towards a fully developed twin band). The magnitude of the stress overshoot is not sensitive to the loading angle ϕ_{L} and is always about 500 MPa. The stress plateau corresponds to the growth of the twin band (twin thickening). In general, the slope of the stress plateau indicates the extent of strain hardening, which increases as the loading angle ϕ_{L} increases. However, as it is evident in Fig. 9(a), see also Fig. 10, the case with $\phi_{\mathrm{L}} = 45°$ does not follow this rule, and the associated mechanical response exhibits some unique features, which can be attributed to the extra symmetry of the periodic twin microstructure, resulting from the special loading angle $\phi_{\mathrm{L}} = 45°$. Completion of the twinning transformation in the entire simulation domain is manifested by a sharp stress rise in the mechanical response. Note that this stress rise corresponds to a sharp drop of individual stress components, which is associated with the annihilation of twin interfaces, and it is seen as an increase of the equivalent stress $\bar{\sigma}_{\mathrm{eq}}$. The final stage corresponds to the elastoplastic deformation of the fully-twinned domain. Since only one slip system is considered, plastic slip must be accommodated by elastic deformation, hence the high slope of this branch.

Additional simulations have been performed using the multiplicative form of $\mathbf{F}_{\mathrm{in}}$, Eqs. (22)–(24), instead of the additive decomposition of $\mathbf{L}_{\mathrm{in}}$ according to Eq. (20). The corresponding results indicate that, except for some minor changes observed for the loading angle $\phi_{\mathrm{L}} = 45°$, see Fig. 10, the twin evolution and the mechanical response for all loading angles are practically the same as those obtained for the reference model. Fig. 10 suggests that the minor changes originate from the local reverse twinning (detwinning), indicated by the arrows in Fig. 10(b), which may have occurred spuriously as a result of the multiplicative form of $\mathbf{F}_{\mathrm{in}}$ that does not treat detwinning correctly.

A parametric study is performed next with the aim to assess the effect that two crucial model parameters, the hardening parameter H and the interface thickness parameter ℓ, have on the simulation results. The effect of the hardening parameter H on the deformation pattern is qualitatively similar to that of the interface thickness parameter ℓ within the range of the parameters investigated here. More specifically, the lower the parameter ℓ (the parameter H), the stronger the activity of the basal slip, which accordingly may influence the twin microstructure locally. Fig. 11 depicts the effect of ℓ on the microstructure for the loading angle $\phi_{\mathrm{L}} = 22.5°$ at the macroscopic equivalent strain of $\bar{\varepsilon}_{\mathrm{eq}} = 0.045$ (a separate figure showing a similar effect of H on the microstructure is not provided). It can be seen that, although the activity of the basal slip is quite different for various ℓ, the general features of the twin microstructure are preserved for all values of ℓ. Another important aspect concerns the effect of the interface thickness parameter ℓ on the actual thickness of the diffuse matrix–twin interface. For a better visualization of the interface thickness, the twin microstructure is additionally represented in Fig. 11 by the spatial distribution of the order parameter η.

The parameters H and ℓ have quite a different impact on the stress–strain response, see Fig. 9(b,c). The interface thickness parameter ℓ has a direct impact on the nucleation stress. The lower the parameter ℓ, the higher the magnitude of the stress overshoot,
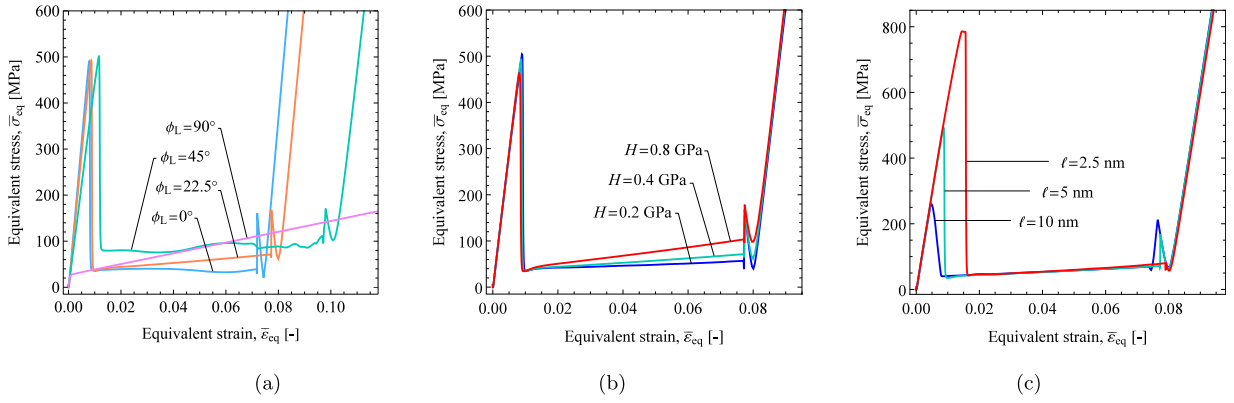
Fig. 9. The macroscopic stress–strain response of the single crystal under proportional isochoric tension–shear loading: (a) for various loading angles ϕ_L, (b) for various hardening parameters H, and (c) for various interface thickness parameters ℓ. The effect of the parameters H and ℓ is shown for the loading angle $\phi_L = 22.5°$.
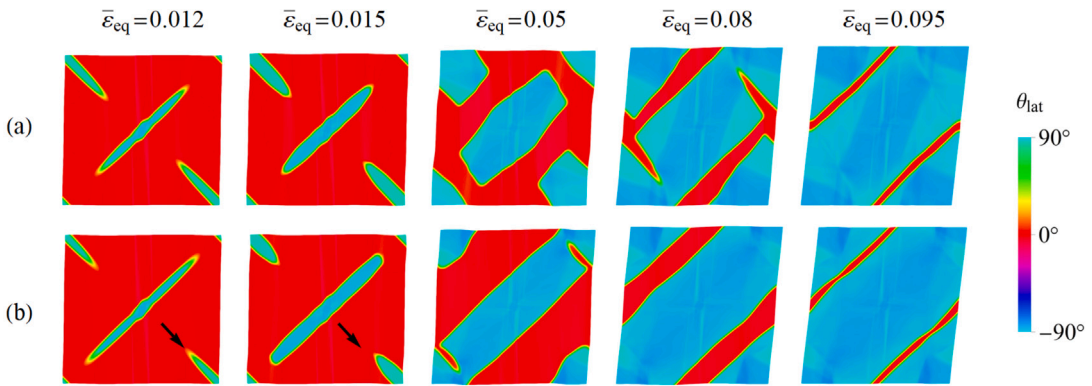

Fig. 10. The effect of the kinematics of the inelastic deformation gradient $\mathbf{F}_{in}$ on the evolution of the twin microstructure for $\phi_L = 45°$: (a) the reference model with $\mathbf{F}_{in}$ of the form (20); (b) the model with the multiplicative form of $\mathbf{F}_{in}$, Eq. (22).
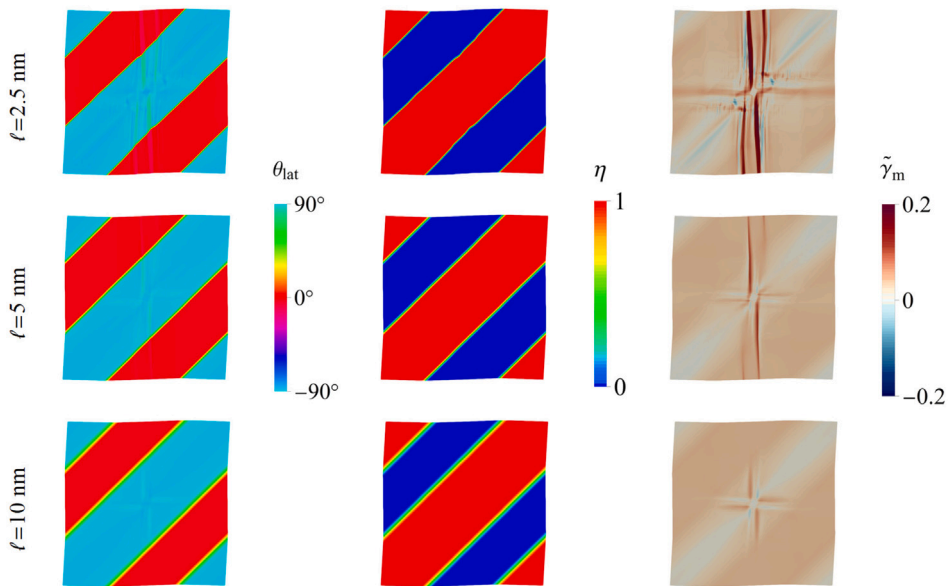
Fig. 11. The effect of the interface thickness parameter ℓ on the twin microstructure (lattice orientation angle θ_{lat}, left), the actual thickness of the matrix–twin diffuse interfaces (order parameter η, center), and the activity of the basal slip in the matrix (effective slip $\tilde{\gamma}_m$, right) for the loading angle $\phi_L = 22.5°$.

indicating a higher energy barrier for the nucleation of the twin, see Eq. (30). At the same time, the hardening parameter H does not have a considerable impact on the nucleation stress, and only affects the slope of the stress plateau.

5.4. Study #3: twin transmission across grain boundary

An important step in the study of deformation twinning is understanding the phenomenon of twin transmission across the grain boundary, which is an essential prerequisite to gain more insight into the twin nucleation, variant selection and propagation processes in polycrystals (Beyerlein et al., 2010; Khosravani et al., 2015; Arul Kumar et al., 2016; Shi et al., 2017). Modeling the phenomenon of twin transmission has been the focus of various studies (e.g., Qiao et al., 2016; Liu et al., 2018a, 2019; Hu et al., 2020, 2021), as a means to explain the mechanism behind the twin nucleation and twin–slip interaction at the grain boundary, and also, from a modeling standpoint, as a suitable benchmark problem to test the capabilities of the modeling approaches. Therefore, the aim of the present study is to investigate the phenomenon of twin transmission in a bi-crystal system with the grain misorientation angle ϕ_{mis} (the angle formed between the [0001]-axis of the two grains in the initial state), as the main controlling parameter, varied systematically (Beyerlein et al., 2011; El Kadiri et al., 2013; Shi et al., 2017; Wang et al., 2018). As a follow-up of the parametric study in Section 5.3, the effect of the hardening parameter H and the interface thickness parameter ℓ is also examined.

The problem setup is shown in Fig. 4(c). The bi-crystal system under study consists of two grains with equal dimensions. The initial lattice orientation of grain 1 is fixed, with the corresponding [0001]-axis aligned with the global x_2-axis, while that of grain 2 varies so that the grain misorientation angle ϕ_{mis} lies within the range $[-40°, 40°]$ with the step of $10°$. A separate field of the micromorphic variable, the counterpart of the order parameter, is introduced for each grain, and a homogeneous Neumann boundary condition is enforced for each variable along the grain boundary. Accordingly, twinning in the two grains is independent, and the interaction between the twins, including twin nucleation in grain 2, is only through the stress field.

The size of the computational domain is set to $w \times h = 2 \times 2 \ \mu m^2$. The domain is uniformly discretized with the finite-element mesh consisting of 160 000 elements (element size of 5 nm), which results in approximately 1.1 million degrees of freedom. On account of increasing the size of the computational domain and the element size with respect to the studies in Sections 5.2 and 5.3, the thickness of the matrix–twin diffuse interface is also increased, i.e., the interface thickness parameter is adopted as $\ell = 10$ nm. Accordingly, to have proportionally equivalent viscous effects, in view of Eq. (46), the reference twinning propagation speed is taken as $v_0 = 200$ nm/s. The other model parameters are the same as those specified in Section 5.1. The bi-crystal is subjected to isochoric tension ($\phi_{\mathrm{L}} = 0$) with a constant macroscopic strain rate of $\bar{d} = 0.01 \ \mathrm{s}^{-1}$. The loading is continued up to the maximum macroscopic equivalent strain of $\bar{\varepsilon}_{\mathrm{eq}} = 0.03$. A twin nucleus in the shape of an inclined ellipse, with the semi-major axis of 20 nm, has been embedded into the center of grain 1, see Fig. 4(c). Like in the study in Section 5.3, the basal slip is considered as the only operative slip system.

Figs. 12 and 13 illustrate the twin transmission behavior in terms of, respectively, the microstructure visualized using the lattice orientation angle θ_{lat} and the associated activity of the basal slip in the matrix for different grain misorientation angles ϕ_{mis}. The activity of the basal slip in the twin is relatively small compared to that in the matrix, so the corresponding snapshots are not provided. The main observation is that the larger the magnitude of the grain misorientation angle ϕ_{mis}, the less likely it is for the twin to transmit across the grain boundaries. When the grain misorientation angle is low, namely $\phi_{\mathrm{mis}} = \pm 10°$, the twin transmits to grain 2 almost immediately after impinging at the grain boundary. The twin transmission is deferred for grain misorientation angles of $\phi_{\mathrm{mis}} = \pm 20°$ and $\phi_{\mathrm{mis}} = -30°$, and finally, no twin transmission occurs for $\phi_{\mathrm{mis}} = 30°$ and $\phi_{\mathrm{mis}} = \pm 40°$. The natural explanation for this behavior is that the Schmid factor for basal slip increases with increasing magnitude of ϕ_{mis}, while that for twinning decreases, which makes the basal slip a more favorable deformation mechanism compared to twinning. The twin transmission behavior depends not only on the magnitude but also on the sign of the grain misorientation angle ϕ_{mis}. As shown in Fig. 12, the cutoff misorientation angle (defined as the misorientation angle at which the twin transmission ceases to occur) for positive and negative ϕ_{mis} is obtained as $30°$ and $-40°$, respectively. In some cases, the twin transmission into grain 2 proceeds in a discontinuous manner, i.e., the twin nucleation in grain 2 occurs at a short distance from the grain boundary and is accompanied by a relatively high activity of the basal slip in that region, see, e.g., the snapshots related to $\phi_{\mathrm{mis}} = 20°$ and $\phi_{\mathrm{mis}} = -30°$. For some grain misorientation angles, e.g., $\phi_{\mathrm{mis}} = \pm 20°$, as a result of the stress concentration at the grain boundaries, additional twins nucleate that propagate towards the interior of grain 1.

The results of the parametric study in Section 5.3 revealed how and to what extent the hardening parameter H and the interface thickness parameter ℓ impact the microstructure evolution in a single crystal. The most prominent observation noted was that smaller values of H and ℓ induce a more prevalent activity of the basal slip, which in turn may influence the twin microstructure. It is therefore of primary importance to explore the effect of these parameters on the twin transmission behavior. To this end, additional simulations have been carried out for the hardening parameters $H = 0.2$ and 0.8 GPa and the interface thickness parameters $\ell = 5$ and 20 nm. Recall that $H = 0.4$ GPa and $\ell = 10$ nm have been used in the reference simulations reported above. Results show that twin transmission is more difficult for smaller values of H and ℓ. More specifically, for $H = 0.2$ GPa and for $\ell = 5$ nm, twin transmission occurs only for low grain misorientation angles $\phi_{\mathrm{mis}} = \pm 10°$. At the same time, for $H = 0.8$ GPa and for $\ell = 20$ nm, twin transmission is facilitated resulting in cutoff misorientation angles of $\pm 40°$. To give a further elaboration, the effect of H and ℓ for two representative grain misorientation angles $\phi_{\mathrm{mis}} = -20°$ and $\phi_{\mathrm{mis}} = 30°$ is shown in Figs. 14 and 15, respectively. In addition, Fig. 16 depicts the details of the twin microstructure, including the thickness of the diffuse interfaces, for different ℓ. A similar study concerning the effect of the hardening parameter on the twin transmission behavior has been reported by Hu et al. (2021). However, to our knowledge, no previous phase-field study has highlighted and evaluated the significant impact of the thickness of the diffuse twin boundaries on the twin transmission behavior.
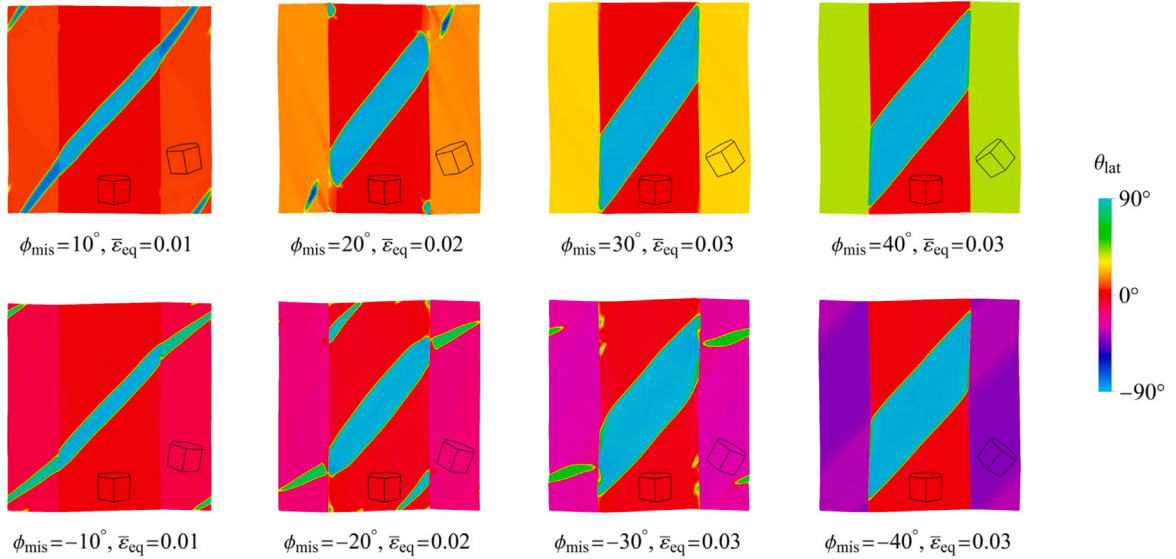
Fig. 12. Twin transmission across the grain boundaries: distribution of the lattice orientation angle θ_{lat} for different grain misorientation angles ϕ_{mis}. Note that the snapshots are taken at different macroscopic equivalent strains $\bar{\varepsilon}_{eq}$.
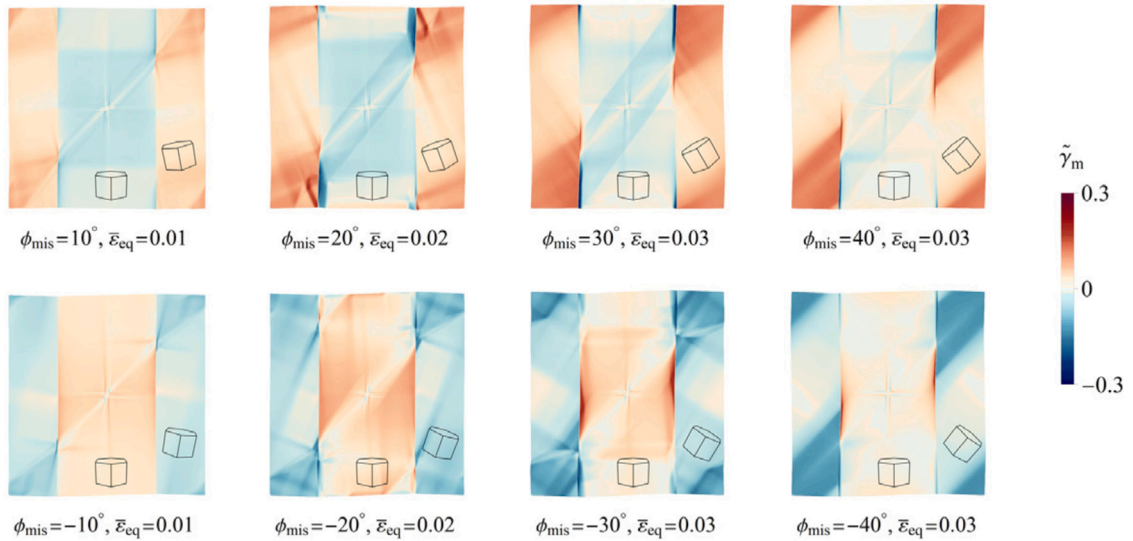

Fig. 13. Twin transmission across the grain boundaries: distribution of the effective basal slip in the matrix, $\tilde{\gamma}_m$, for different grain misorientation angles ϕ_{mis}. Note that the snapshots are taken at different macroscopic equivalent strains $\bar{\varepsilon}_{eq}$ (the same as in Fig. 12).

The results of the parametric study presented above and that in Section 5.3 demonstrate the key role of the hardening parameter H and the interface thickness parameter ℓ on the simulation results. An important conclusion is that the selection of these parameters must be done with a particular attention, as it may lead to physically unacceptable predictions. For instance, excessively large values of ℓ result in unduly diffuse twin interfaces and partially transformed regions, see the snapshot related to $\ell = 20$ nm in Fig. 16.

5.5. Study #4: microstructure evolution in a 10-grain unit cell

The studies presented above highlighted some specific features of the model and displayed the model predictions in idealized single-crystal and bi-crystal setups. In the last study presented here, we address a more complex scenario of a unit cell containing 10 grains. A twofold goal is pursued. On the one hand, to use the 10-grain setup as a template to demonstrate the modeling capabilities in terms of the microstructure evolution in a challenging computational problem. On the other hand, to qualitatively capture some microstructural features observed in the experiments. Modeling of the spatially-resolved twin microstructure evolution
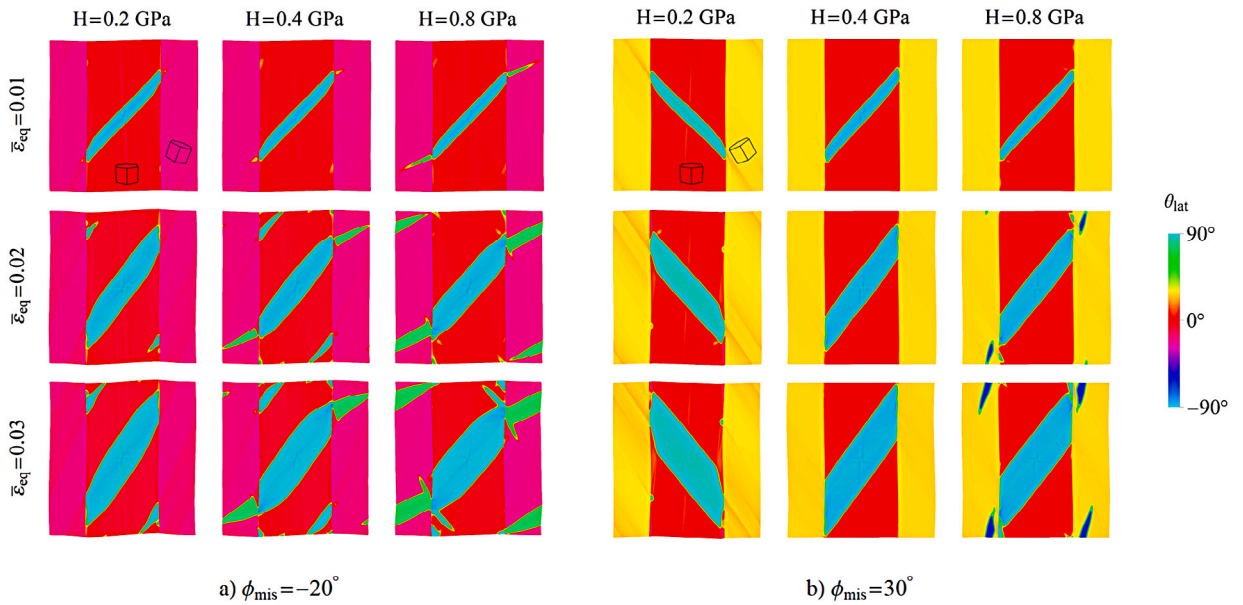
Fig. 14. The effect of the hardening parameter H on the twin transmission across the grain boundaries for the grain misorientation angles (a) $\phi_{\mathrm{mis}} = -20°$, and (b) $\phi_{\mathrm{mis}} = 30°$.
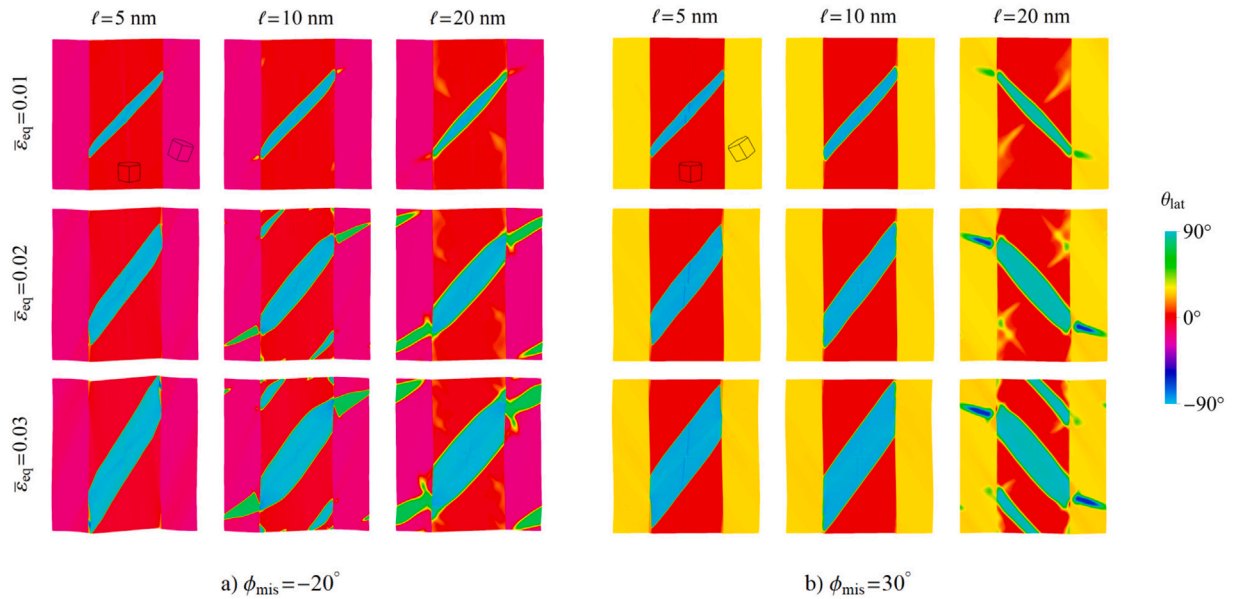

Fig. 15. The effect of the interface thickness parameter ℓ on the twin transmission across the grain boundaries for the grain misorientation angles (a) $\phi_{\mathrm{mis}} = -20°$, and (b) $\phi_{\mathrm{mis}} = 30°$.

in polycrystalline magnesium has been the subject of some recent studies, including those based on the phase-field method (e.g., Liu et al., 2018a,b; Ma and Sun, 2021; Hu et al., 2021) and using other approaches (e.g., Mareau and Daymond, 2016; Cheng et al., 2018, 2021).

The problem setup is shown in Fig. 17(a). A unit cell containing 10 grains with the dimensions of $w \times h = 5 \times 5 \ \mu\mathrm{m}^2$ is considered. The initial periodic microstructure is generated via Voronoi tessellation technique. Despite the limitations of the Voronoi technique (Ardeljan et al., 2015), care has been taken to spatially arrange the Voronoi seeds in a way to optimize the shape of the grains, and thus to achieve a possibly realistic grain microstructure. The initial lattice orientation of each grain, i.e., the orientation of the local [0001]-axis, is assigned randomly within the range [−90°, 90°]. Since a uniform finite-element mesh is used, an element is assigned to a specific grain when the element center belongs to the respective Voronoi cell. The grain boundaries have thus a
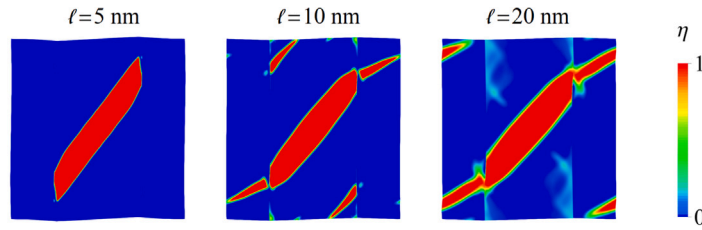
Fig. 16. The effect of the interface thickness parameter ℓ on the actual thickness of the matrix–twin diffuse interface in the study of twin transmission. The snapshots correspond to the grain misorientation angle $\phi_{\text{mis}} = -20°$ taken at the macroscopic equivalent strain of $\bar{\varepsilon}_{\text{eq}} = 0.02$, see Fig. 15(a).
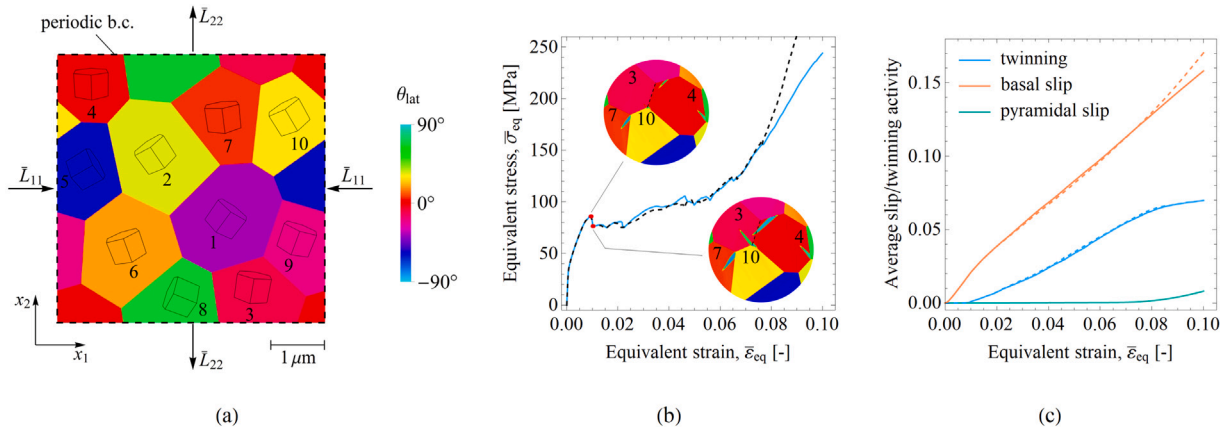

Fig. 17. (a) The initial periodic microstructure of the 10-grain unit cell under study. (b) The resulting overall mechanical response expressed in terms of the macroscopic equivalent stress and strain. The insets show the twin nucleation events corresponding to the instants of the first stress overshoot and stress drop. (c) The average activity of the individual deformation mechanisms during the simulation. The dashed curves in panels (b) and (c) represent the corresponding results obtained for the simulation with no pyramidal slip.

stepped appearance. As in the bi-crystal problem in Section 5.4, a separate micromorphic variable is introduced for each grain with a homogeneous Neumann boundary condition along the grain boundary. No twin nuclei are introduced, and twin nucleation is triggered solely by the inhomogeneous stress state that develops in the polycrystal upon loading, see Remark 3.1.

The 10-grain unit cell is subjected to isochoric tension ($\phi_{\text{L}} = 0$) at a constant macroscopic strain rate of $\bar{d} = 0.01 \text{ s}^{-1}$. The interface thickness parameter of $\ell = 10$ nm and the reference twinning propagation speed of $v_0 = 500$ nm/s have been used. The latter, based on the results of our auxiliary simulations, leads to relatively small viscous effects, and thus, does not affect noticeably the resulting twin microstructure and the mechanical response. The remaining material parameters are the same as those in Section 5.1. In order to correctly reproduce the fine features of the microstructure, a finite-element mesh with the element size of 6.25 nm has been adopted, leading to 650 000 elements and nearly 5 million degrees of freedom. Unlike in the previous studies, all three slip systems, namely one basal and two pyramidal slip systems, are considered operative. The simulation has been run up to the macroscopic equivalent strain of $\bar{\varepsilon}_{\text{eq}} = 0.1$.

Figs. 17(b) and 18 illustrate, respectively, the overall mechanical response of the 10-grain unit cell and the snapshots of the twin microstructure evolution (a movie showing the complete microstructure evolution is provided as a supplementary material). The important microstructural events, such as twin nucleation, twin impinging at the grain boundary, coalescence of the twinned regions and the completion of the twin transformation in a grain, are marked by sudden stress changes. At the onset of twinning (around $\bar{\varepsilon}_{\text{eq}} = 0.01$), multiple twin nucleations take place at grain boundaries surrounding the grains most favorably oriented for twinning, namely grains 3, 4 and 7, see the insets in Fig. 17(b). Recall that no additional trigger has been introduced at the grain boundaries to assist the twin nucleation. The twin microstructure evolution then proceeds with the growth and transmission of the existing twins, along with the nucleation of new twins (mostly at the grain boundaries). Depending on the initial lattice orientation of the surrounding grains, the twins either grow towards the interior of the grains or along the grain boundaries. In the case of a twin impinging at the grain boundary, twin transmission or twin suppression have been observed, which is primarily determined by the grain misorientation angle. The twin evolution at this stage is accompanied by a plateau-like branch in the overall mechanical response exhibiting a mild strain hardening. Starting from the equivalent strain of about $\bar{\varepsilon}_{\text{eq}} = 0.06$, the hardening starts to gradually increase and twinning starts to saturate in the preferably oriented grains (3,4,7). The increase of the strain hardening can be attributed to decreasing activity of twinning which is compensated by the activity of the pyramidal slip, however, at a higher CRSS. By the end of the simulation (at $\bar{\varepsilon}_{\text{eq}} = 0.1$), 8 out of 10 grains are twinned (either completely or partially), while no sign of twinning can be discerned within the grains not suitably oriented for twinning, namely grains 5 and 8.
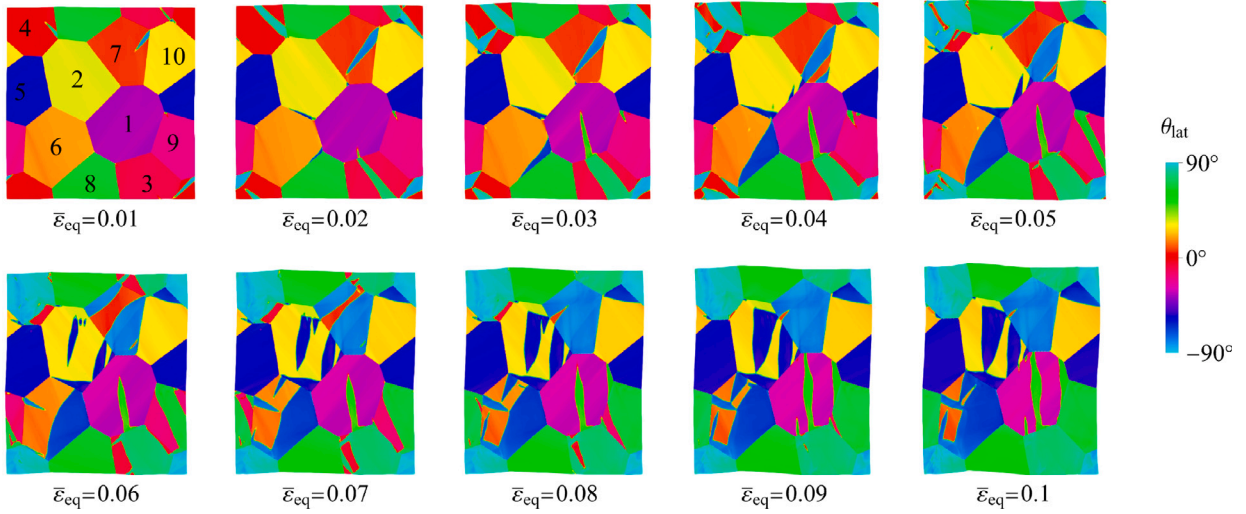
Fig. 18. Snapshots of the twin microstructure evolution represented by the lattice orientation angle θ_{lat} in the 10-grain unit cell.
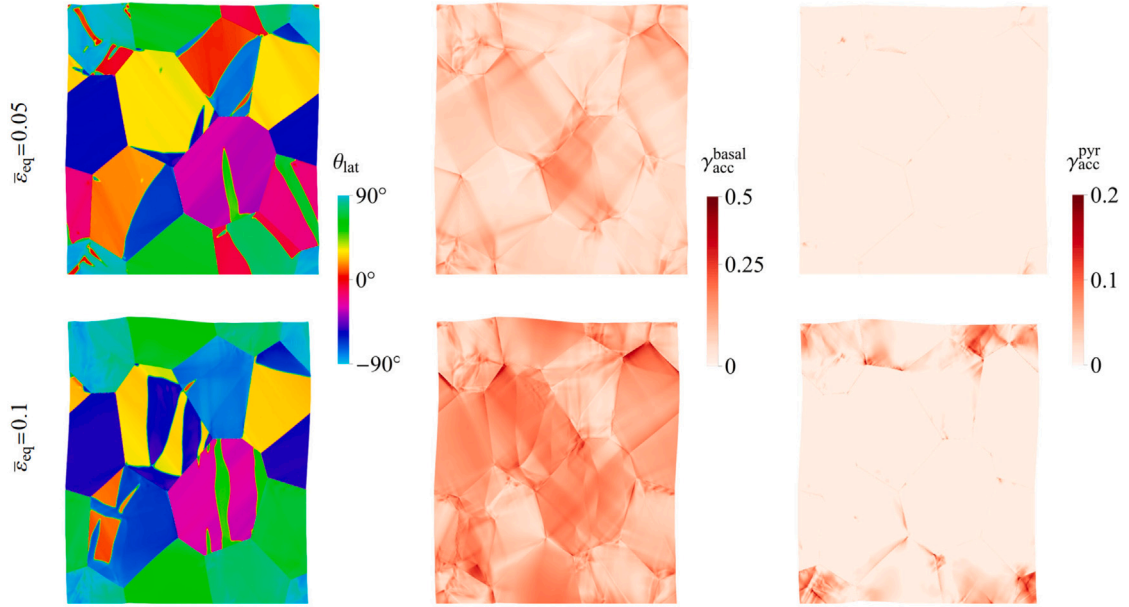

Fig. 19. Snapshots of the twin microstructure, accumulated basal slip $\gamma_{\text{acc}}^{\text{basal}}$, and accumulated pyramidal slip $\gamma_{\text{acc}}^{\text{pyr}}$ at two representative macroscopic equivalent strains, $\bar{\varepsilon}_{\text{eq}} = 0.05$ and $\bar{\varepsilon}_{\text{eq}} = 0.1$. Note the different scale used for $\gamma_{\text{acc}}^{\text{basal}}$ and $\gamma_{\text{acc}}^{\text{pyr}}$.

To gain a more comprehensive understanding of the deformation behavior, the contribution of the individual deformation mechanisms needs to be identified. For this, the snapshots of the twin microstructure, accumulated basal slip $\gamma_{\text{acc}}^{\text{basal}}$, and accumulated pyramidal slip $\gamma_{\text{acc}}^{\text{pyr}}$ (resulting from both pyramidal slip systems) are shown in Fig. 19 for two representative macroscopic equivalent strains, namely $\bar{\varepsilon}_{\text{eq}} = 0.05$ and $\bar{\varepsilon}_{\text{eq}} = 0.1$. The accumulated slips, $\gamma_{\text{acc}}^{\text{basal}}$ and $\gamma_{\text{acc}}^{\text{pyr}}$, are computed according to Eq. (26) by considering only the respective slip systems. In addition, to make a quantitative evaluation, the average activity of the individual deformation mechanisms is plotted in Fig. 17(c). The average twinning and slip activities are calculated, respectively, as the volume average of the effective twinning shear ($\eta\gamma_{\text{tw}}$) and the accumulated slip ($\gamma_{\text{acc}}^{\text{basal}}$ or $\gamma_{\text{acc}}^{\text{pyr}}$) over the entire simulation domain. The results, unsurprisingly, indicate that within the range of the macroscopic strain considered here, both twinning and basal slip mechanisms exhibit strong activity. The activity of the basal slip is, in particular, more pronounced, and the corresponding average activity follows a roughly linear trend. On the other hand, the pyramidal slip contribution to the overall plastic deformation is found to be noticeable only at the final stage of loading, when some of the grains are largely twinned. The results presented here are in a qualitative agreement with the related previous studies (Wang et al., 2010b; Cheng et al., 2018; Hu et al., 2021).
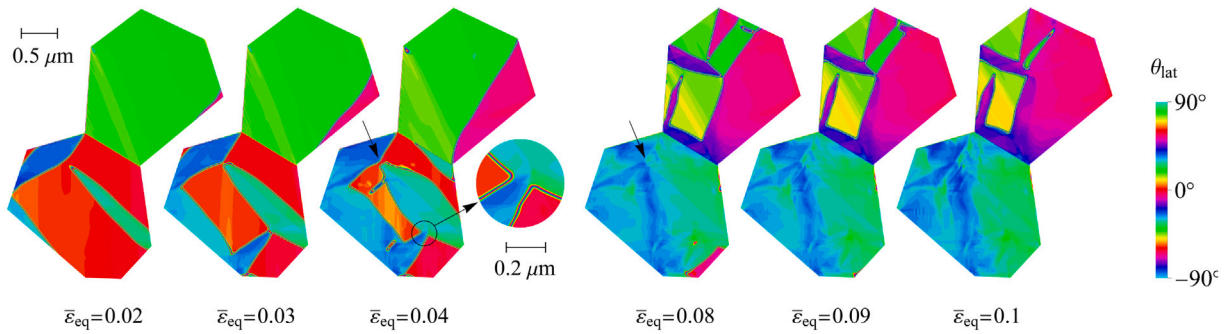
Fig. 20. Detailed view of the lattice orientation in grains 4 and 6 (shown in the reference configuration) illustrating the interaction of conjugate twins. The lattice orientation angle θ_{lat} is depicted using a high-resolution color scale; for the actual orientation refer to Fig. 18.

To highlight the role of the pyramidal slip systems, an additional simulation has been performed with no pyramidal slip systems involved, see the dashed lines in Fig. 17(b,c). It follows that the twin microstructure evolution and the overall mechanical response are qualitatively similar to those of the reference simulation (with pyramidal slip systems). In particular, the mechanical response follows a similar trend as that of the reference case up to the point where grain 4 is entirely transformed to the twin (at $\bar{\varepsilon}_{\mathrm{eq}} = 0.08$), and thereafter advances with a higher level of stress, which is obviously due to the lack of the pyramidal slip mechanism.

A careful analysis of the simulation results reveals several interesting microstructural features, some of them resemble those observed in experiments. Here, we briefly comment some of the predicted features that can be noticed in Figs. 17–19, see also the supplementary movie. In most cases, twins nucleate at grain boundaries, which is a common feature observed in experiments (e.g., Beyerlein et al., 2010) and is often explicitly prescribed in phase-field simulations (e.g., Liu et al., 2018b). However, in grain 2, the basal slip originating from the grain boundaries acts as a precursor for twin nucleation in the interior of the grain, see the snapshot corresponding to $\bar{\varepsilon}_{\mathrm{eq}} = 0.06$ in Fig. 18. It has been observed that the twins propagating towards the interior of the grains (not along the grain boundaries) have a lenticular shape, which is generally the most widely observed shape for the twins in the experiments (Arul Kumar et al., 2019). Grain 1 is not oriented favorably for twinning (the initial orientation angle is about $-35°$), however, it twins partially, mostly through the twin nucleating at the boundary with grain 3, to accommodate local stresses. At the same time, strong basal slip is generated in grain 1, see Fig. 19, to relax the stresses produced at the tips of the twins impinged at the surrounding grain boundaries. Such twin–slip interaction has been observed at a larger scale by Barnett et al. (2013). It can also be seen that, due to the strong activity of the basal slip in grain 1, the twin propagating in this grain is (temporarily) arrested in the interior of the grain (cf. Yaddanapudi et al., 2021).

Finally, twin–twin interaction between conjugate twins has been observed in a number of grains. In particular, grains 4 and 6 exhibit a hierarchy of twin–twin interaction events, as illustrated in more detail in Fig. 20. It can be seen that the newly-formed twins that run towards the twin boundary of an existing twin cause the twin boundary to tilt slightly towards the approaching twin tip, in agreement with the experiment (Yu et al., 2014) and other phase-field studies (Hu et al., 2021). The difference in the lattice orientation of the conjugate twins is apparent in Fig. 20 thanks to the high-resolution color scale used. The difference in orientation persists after the two twins merge (recall that a single order parameter is used to represent both conjugate twins). This is visible, for instance, in grain 4 at the location indicated by the arrows and also at another location shown in the inset. In the case of conjugate twins, the twin–twin boundary is a low-angle tilt boundary (Yu et al., 2014), and the steep gradient of the lattice orientation at these two locations can be interpreted as such a low-angle tilt boundary, here having a somewhat diffuse appearance resulting from the diffuse-interface framework. Interestingly, the apparent twin–twin boundary shown in the inset has a characteristic V-shape appearance observed in the experiment and explained by the mechanisms of zipping and dissociating (see Yu et al., 2014, Fig. 7).

6. Conclusion

A finite-strain model of coupled deformation twinning and plastic slip has been developed in this work by combining the phase-field method and the crystal plasticity framework. The formulation is based on the incremental energy minimization approach, and the model is discretized by means of the finite-element method. The implementation is facilitated by resorting to the micromorphic formulation so that the complex constitutive equations, including the evolution equation for the order parameter, are solved at the Gauss-point level, while, on the global level, a Helmholtz-type PDE is solved for the micromorphic variable approximating the order parameter. The resulting computational model allows simulation of spatially resolved evolution of twin microstructure, as illustrated by a number of 2D computational studies.

As an important step towards model development, a detailed discussion of the finite-strain kinematics of deformation twinning has been carried out considering both sharp- and diffuse-interface descriptions. It has been shown that twinning can be treated as a displacive transformation, similar to a martensitic phase transformation, in which the parent phase (matrix) may transform to one of several twin deformation variants, each characterized by a volume-preserving stretch tensor. Each twin deformation variant represents then two conjugate twinning systems, where, in the conventional approach, each crystallographic twinning system

is characterized by a simple shear deformation. This simple shear deformation includes a rigid-body rotation that results from crystallography and corresponds to the theoretical orientation of the interface and to stress-free conditions. In the stretch-based kinematics, the rigid-body rotation is a part of the solution of the problem and is included in the elastic part of the deformation gradient. Note that the rotation may differ from the theoretical one when the orientation of the twin interface differs from the theoretical one, e.g., at the tip of a twin plate, and when the material is under stress.

The two approaches are equivalent in the sharp-interface description, also when plastic slip is considered as an additional inelastic deformation mechanism, and the only difference is then in a relative rotation of the respective local intermediate configurations. However, the equivalence does not necessarily hold in the diffuse-interface description. The stretch-based kinematics, advocated in this work, is particularly convenient for phase-field modeling of twinning since a single order parameter can be used to describe one twin deformation variant such that the corresponding two conjugate twinning systems are treated equally (this feature is illustrated by one of the numerical examples). Moreover, the notion of the intermediate isoclinic configuration is naturally embedded into the stretch-based scheme.

To fix attention, detailed derivations have been provided for $\{10\bar{1}2\}\langle\bar{1}011\rangle$ tensile twinning in HCP magnesium alloys, but the related features discussed above are more general and apply also to other cases, in particular, to $\{111\}\langle11\bar{2}\rangle$ twinning in FCC crystals and to $\{112\}\langle\bar{1}\bar{1}1\rangle$ twinning in BCC crystals. The proposed phase-field model and its variational formulation are also general, even if the computational model has been developed specifically for magnesium, moreover, limited to the 2D plane-strain conditions with one twin deformation variant (thus with two conjugate twinning systems) and with three equivalent in-plane slip systems (one basal and two pyramidal). Extension to the general 3D case would be rather straightforward, except the high computational cost.

A number of 2D plane-strain problems have been studied to illustrate the capabilities of the proposed model. To focus on the most important features, some simplifying assumptions have been adopted, in particular, concerning hardening behavior, but otherwise physically relevant model parameters have been adopted in the computations. Idealized single-crystal and bi-crystal setups have been used to illustrate features such as the equal treatment of the conjugate twinning systems in the stretch-based kinematics, twin–slip interaction, and twin transmission across the grain boundaries. As an application to a more challenging problem, twin microstructure evolution has been studied in a unit cell containing 10 grains. Several noteworthy microstructural features have been captured, some of which are in agreement with those observed in experiments and predicted in other phase-field studies.

CRediT authorship contribution statement

Mohsen Rezaee-Hajidehi: Methodology, Software, Writing – original draft, Writing – review & editing, Visualization. **Przemysław Sadowski:** Methodology, Software. **Stanisław Stupkiewicz:** Conceptualization, Methodology, Writing – review & editing, Supervision.

Declaration of competing interest

The authors declare that they have no known competing financial interests or personal relationships that could have appeared to influence the work reported in this paper.

Acknowledgments

Appendix A. Stretch-based kinematics of twinning in FCC and BCC crystals

A.1. $\{111\}\langle11\bar{2}\rangle$ twinning in FCC crystals

The $\{111\}\langle11\bar{2}\rangle$ twinning in FCC crystals involves 12 twinning systems that form 6 pairs of conjugate twinning systems. The stretch-based kinematics is here illustrated for a representative pair, specifically for the $(111)[11\bar{2}]$ and $(11\bar{1})[112]$ twinning systems that are shown in Fig. A.1(a–c). The corresponding twin plane normal, twinning shear direction, and twinning shear are specified as (Christian and Mahajan, 1995)

$$\mathbf{m}^{(1,2)} = \frac{1}{\sqrt{3}}(\mp1, \mp1, 1), \qquad \mathbf{a}^{(1,2)} = \frac{1}{\sqrt{6}}(\mp1, \mp1, -2), \qquad \gamma_{\text{tw}} = \frac{1}{\sqrt{2}}, \tag{A.1}$$

with the components given in the cubic basis of the matrix. By following the procedure described in Section 2.2, the twinning stretch $\mathbf{U}_{\text{tw}}$ and rotation $\mathbf{R}_{\text{tw}}$, see Eqs. (5)–(8), are found in the following form,

$$\mathbf{U}_{\text{tw}} = \frac{1}{2}\begin{pmatrix} \sqrt{2}+1 & \sqrt{2}-1 & 0 \\ \sqrt{2}-1 & \sqrt{2}+1 & 0 \\ 0 & 0 & \sqrt{2} \end{pmatrix}, \qquad \mathbf{R}_{\text{tw}} = \frac{1}{6}\begin{pmatrix} 2\sqrt{2}+3 & 2\sqrt{2}-3 & -\sqrt{2} \\ 2\sqrt{2}-3 & 2\sqrt{2}+3 & -\sqrt{2} \\ \sqrt{2} & \sqrt{2} & 4\sqrt{2} \end{pmatrix}. \tag{A.2}$$

The $(1\bar{1}0)$ plane is the plane of shear, and this plane is shown in Fig. A.1(b,c). It can be seen that the stretch $\mathbf{U}_{\text{tw}}$ corresponds to elongation by $\sqrt{2}$ along the [110] axis and contraction by $1/\sqrt{2}$ along the [001] axis. The twinning transformation and the subsequent

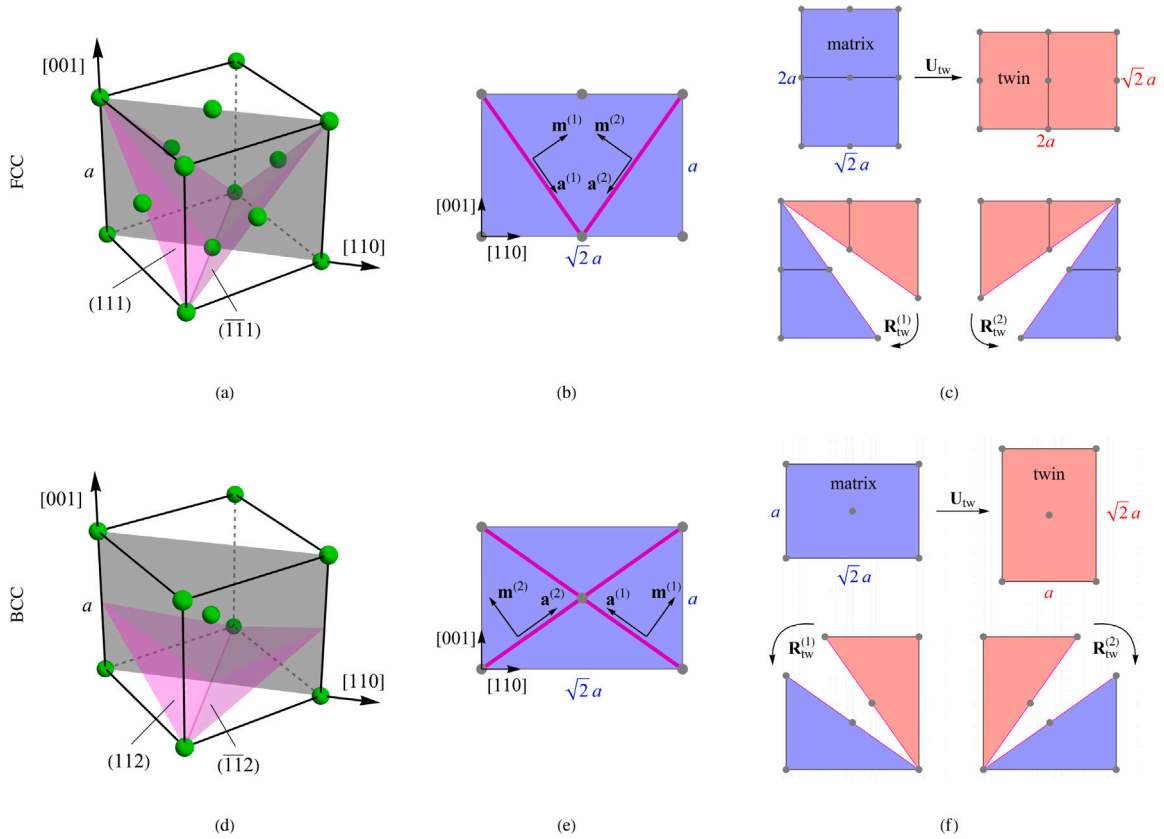**Fig. A.1.** Illustration of the $\{111\}\langle11\bar{2}\rangle$ twinning in FCC crystals (a–c) and $\{112\}\langle\bar{1}\bar{1}1\rangle$ twinning in BCC crystals (d–f): (a,d) unit cell with the twin planes of one pair of conjugate twinning systems; (b,e) conjugate twinning systems shown in the $(1\bar{1}0)$ plane; (c,f) stretch-based kinematics of twinning.

rotation are illustrated in Fig. A.1(c) using the section of two crystallographic unit cells by the $(1\bar{1}0)$ plane so that the section has the dimensions of $\sqrt{2}a \times 2a$.

The stretch tensors of the remaining 5 pairs of conjugate twinning systems can be obtained in an analogous way or, equivalently, by applying rotations from the point group of the cubic lattice. It turns out that the resulting stretch tensors of the six twin deformation variants have exactly the same form as the transformation stretches of the six variants of martensite in the cubic-to-orthorhombic transformation with the stretch parameters $\alpha = \sqrt{2}$, $\beta = 1/\sqrt{2}$, and $\gamma = 1$, see Bhattacharya (2003).

A.2. $\{112\}\langle\bar{1}\bar{1}1\rangle$ twinning in BCC crystals

The $\{112\}\langle\bar{1}\bar{1}1\rangle$ twinning in BCC crystals also involves 12 twinning systems that form 6 pairs of conjugate twinning systems. The kinematics is here illustrated using the $(112)[\bar{1}\bar{1}1]$ and $(\bar{1}\bar{1}2)[111]$ twinning systems that are shown in Fig. A.1(d–f). The corresponding twin plane normal, twinning shear direction, and twinning shear are specified as (Christian and Mahajan, 1995)

$$\mathbf{m}^{(1,2)} = \frac{1}{\sqrt{6}}(\mp1, \mp1, 2), \qquad \mathbf{a}^{(1,2)} = \frac{1}{\sqrt{3}}(\pm1, \pm1, 1), \qquad \gamma_{\text{tw}} = \frac{1}{\sqrt{2}}, \tag{A.3}$$

with the components given in the cubic basis of the matrix. The twinning stretch $\mathbf{U}_{\text{tw}}$ and rotation $\mathbf{R}_{\text{tw}}$ are now found in the following form,

$$\mathbf{U}_{\text{tw}} = \frac{1}{4}\begin{pmatrix} \sqrt{2}+2 & \sqrt{2}-2 & 0 \\ \sqrt{2}-2 & \sqrt{2}+2 & 0 \\ 0 & 0 & 4\sqrt{2} \end{pmatrix}, \qquad \mathbf{R}_{\text{tw}} = \frac{1}{6}\begin{pmatrix} 2\sqrt{2}+3 & 2\sqrt{2}-3 & \sqrt{2} \\ 2\sqrt{2}-3 & 2\sqrt{2}+3 & \sqrt{2} \\ -\sqrt{2} & -\sqrt{2} & 4\sqrt{2} \end{pmatrix}. \tag{A.4}$$

Note that the rotation tensor $\mathbf{R}_{\text{tw}}$ in Eq. (A.4) is the transpose of that in Eq. (A.2).

The plane of shear is here also the $(1\bar{1}0)$ plane, and this plane is shown in Fig. A.1(e,f). The stretch $\mathbf{U}_{\text{tw}}$ corresponds now to contraction by $1/\sqrt{2}$ along the [110] axis and elongation by $\sqrt{2}$ along the [001] axis.

As in the case of FCC crystals, the transformation stretches of the six twin deformation variants have the same form as those in the cubic-to-orthorhombic transformation, now with the stretch parameters $\alpha = 1/\sqrt{2}$, $\beta = \sqrt{2}$, and $\gamma = 1$.

Appendix B. Supplementary data

Supplementary material related to this article can be found online at https://doi.org/10.1016/j.jmps.2022.104855.

References

Agarwal, G., Dongare, A.M., 2019. Deformation twinning in polycrystalline Mg microstructures at high strain rates at the atomic scales. Sci. Rep. 9, 1–11.

Agnew, S.R., Tomé, C.N., Brown, D.W., Holden, T.M., Vogel, S.C., 2003. Study of slip mechanisms in a magnesium alloy by neutron diffraction and modeling. Scripta Mat. 48, 1003–1008.

Agnew, S.R., Yoo, M.H., Tome, C.N., 2001. Application of texture simulation to understanding mechanical behavior of Mg and solid solution alloys containing Li or Y. Acta Mater. 49, 4277–4289.

Akhtar, A., Teghtsoonian, E., 1969. Solid solution strengthening of magnesium single crystals—I alloying behaviour in basal slip. Acta Metall. 17, 1339–1349.

Al-Samman, T., Gottstein, G., 2008. Room temperature formability of a magnesium AZ31 alloy: Examining the role of texture on the deformation mechanisms. Mater. Sci. Eng. A 488, 406–414.

Alart, P., Curnier, A., 1991. A mixed formulation for frictional contact problems prone to Newton like solution methods. Comput. Methods Appl. Mech. Engrg. 92, 353–375.

Allen, S.M., Cahn, J.W., 1979. A microscopic theory for antiphase boundary motion and its application to antiphase domain coarsening. Acta Metall. 27, 1085–1095.

Ardeljan, M., McCabe, R.J., Beyerlein, I.J., Knezevic, M., 2015. Explicit incorporation of deformation twins into crystal plasticity finite element models. Comput. Methods Appl. Mech. Engrg. 295, 396–413.

Arul Kumar, M., Beyerlein, I.J., McCabe, R.J., Tome, C.N., 2016. Grain neighbour effects on twin transmission in hexagonal close-packed materials. Nat. Commun. 7, 1–9.

Arul Kumar, M., Capolungo, L., McCabe, R.J., Tomé, C.N., 2019. Characterizing the role of adjoining twins at grain boundaries in hexagonal close packed materials. Sci. Rep. 9, 1–10.

Asaro, R.J., 1983. Micromechanics of crystals and polycrystals. In: Hutchinson, J.W., Wu, T.Y. (Eds.), In: Advances in Applied Mechanics, vol. 23, Elsevier, pp. 1–115.

Ball, J.M., James, R.D., 1987. Fine phase mixtures as minimizers of energy. Arch. Ration. Mech. Anal. 100, 13–50.

Barnett, M.R., Keshavarz, Z., Ma, X., 2006. A semianalytical sachs model for the flow stress of a magnesium alloy. Metall. Mat. Trans. A 37, 2283–2293.

Barnett, M.R., Stanford, N., Ghaderi, A., Siska, F., 2013. Plastic relaxation of the internal stress induced by twinning. Acta Mater. 61, 7859–7867.

Basak, A., Levitas, V.I., 2017. Interfacial stresses within boundary between martensitic variants: Analytical and numerical finite strain solutions for three phase field models. Acta Mater. 139, 174–187.

Beyerlein, I.J., Arul Kumar, M., 2018. The stochastic nature of deformation twinning: application to HCP materials. In: Andreoni, W., Yip, S. (Eds.), In: Handbook of Materials Modeling, Springer Nature, Switzerland.

Beyerlein, I.J., Capolungo, L., Marshall, P.E., McCabe, R.J., Tomé, C.N., 2010. Statistical analyses of deformation twinning in magnesium. Phil. Mag. 90, 2161–2190.

Beyerlein, I.J., McCabe, R.J., Tomé, C.N., 2011. Effect of microstructure on the nucleation of deformation twins in polycrystalline high-purity magnesium: A multi-scale modeling study. J. Mech. Phys. Solids 59, 988–1003.

Beyerlein, I.J., Zhang, X., Misra, A., 2014. Growth twins and deformation twins in metals. Ann. Rev. Mat. Res. 44, 329–363.

Bhattacharya, K., 2003. Microstructure of Martensite: Why It Forms and how It Gives Rise To the Shape-Memory Effect. Oxford University Press, Oxford.

Capolungo, L., Beyerlein, I.J., 2008. Nucleation and stability of twins in hcp metals. Phys. Rev. B 78, 024117.

Capolungo, L., Marshall, P.E., McCabe, R.J., Beyerlein, I.J., Tomé, C.N., 2009. Nucleation and growth of twins in Zr: a statistical study. Acta Mater. 57, 6047–6056.

Chang, Y., Kochmann, D.M., 2015. A variational constitutive model for slip-twinning interactions in hcp metals: Application to single- and polycrystalline magnesium. Int. J. Plast. 73, 39–61.

Chapuis, A., Driver, J.H., 2011. Temperature dependency of slip and twinning in plane strain compressed magnesium single crystals. Acta Mater. 59, 1986–1994.

Cheng, J., Hu, X., Bong, H.J., Ghosh, S., Sun, X., 2021. A finite element formulation for deformation twinning induced strain localization in polycrystal magnesium alloys. Comput. Mater. Sci. 190, 110323.

Cheng, J., Shen, J., Mishra, R.K., Ghosh, S., 2018. Discrete twin evolution in Mg alloys using a novel crystal plasticity finite element model. Acta Mater. 149, 142–153.

Chester, S.A., Bernier, J.V., Barton, N.R., Balogh, L., Clausen, B., Edmiston, J.K., 2016. Direct numerical simulation of deformation twinning in polycrystals. Acta Mater. 120, 348–363.

Christian, J.W., Mahajan, S., 1995. Deformation twinning. Prog. Mat. Sci. 39, 1–157.

Clayton, J.D., Knap, J., 2011. A phase field model of deformation twinning: nonlinear theory and numerical simulations. Physica D 240, 841–858.

El Kadiri, H., Kapil, J., Oppedal, A.L., Hector Jr., L.G., Agnew, S.R., Cherkaoui, M., Vogel, S.C., 2013. The effect of twin–twin interactions on the nucleation and propagation of $\{10\bar{1}2\}$ twinning in magnesium. Acta Mater. 61, 3549–3563.

Forest, S., 2009. Micromorphic approach for gradient elasticity, viscoplasticity, and damage. J. Eng. Mech. 135, 117–131.

Graff, S., Brocks, W., Steglich, D., 2007. Yielding of magnesium: From single crystal to polycrystalline aggregates. Int. J. Plast. 23, 1957–1978.

Gray, G.T., 2012. High-strain-rate deformation: mechanical behavior and deformation substructures induced. Ann. Rev. Mat. Sci. 42, 285–303.

Grilli, N., Cocks, A.C.F., Tarleton, E., 2020. A phase field model for the growth and characteristic thickness of deformation-induced twins. J. Mech. Phys. Solids 143, 104061.

Hildebrand, F.E., Miehe, C., 2012. A phase field model for the formation and evolution of martensitic laminate microstructure at finite strains. Phil. Mag. 92, 4250–4290.

Hill, R., Rice, J.R., 1972. Constitutive analysis of elastic-plastic crystals at arbitrary strain. J. Mech. Phys. Solids 20, 401–413.

Homayonifar, M., Mosler, J., 2012. Efficient modeling of microstructure evolution in magnesium by energy minimization. Int. J. Plast. 28, 1–20.

Hu, X., Ji, Y., Chen, L., Lebensohn, R.A., Chen, L.-Q., Cui, X., 2021. Spectral phase-field model of deformation twinning and plastic deformation. Int. J. Plast. 143, 103019.

Hu, X., Ji, Y., Heo, T.W., Chen, L.-Q., Cui, X., 2020. Phase-field model of deformation twin-grain boundary interactions in hexagonal systems. Acta Mater. 200, 821–834.

Hudobivnik, B., Korelc, J., 2016. Closed-form representation of matrix functions in the formulation of nonlinear material models. Finite Elem. Anal. Des. 111, 19–32.

Izadbakhsh, A., Inal, K., Mishra, R.K., Niewczas, M., 2011. New crystal plasticity constitutive model for large strain deformation in single crystals of magnesium. Comput. Mater. Sci. 50, 2185–2202.

Jin, T., Mourad, H.M., Bronkhorst, C.A., Beyerlein, I.J., 2019. A single crystal plasticity finite element formulation with embedded deformation twins. J. Mech. Phys. Solids 133, 103723.

Kalidindi, S.R., 1998. Incorporation of deformation twinning in crystal plasticity models. J. Mech. Phys. Solids 46, 267–290.

Kasemer, M., Dawson, P., 2020. A finite element methodology to incorporate kinematic activation of discrete deformation twins in a crystal plasticity framework. Comput. Methods Appl. Mech. Engrg. 358, 112653.

Kelley, E.W., Hosford, W.F., 1968. Plane-strain compression of magnesium and magnesium alloy crystals. Trans. Metall. Soc. AIME 242, 5–13.

Khosravani, A., Fullwood, D.T., Adams, B.L., Rampton, T.M., Miles, M.P., Mishra, R.K., 2015. Nucleation and propagation of $\{10\bar{1}2\}$ twins in AZ31 magnesium alloy. Acta Mater. 100, 202–214.

Kondo, R., Tadano, Y., Shizawa, K., 2014. A phase-field model of twinning and detwinning coupled with dislocation-based crystal plasticity for HCP metals. Comput. Mater. Sci. 95, 672–683.

Korelc, J., Stupkiewicz, S., 2014. Closed-form matrix exponential and its application in finite-strain plasticity. Int. J. Numer. Methods Engrg. 98, 960–987.

Korelc, J., Wriggers, P., 2016. Automation of Finite Element Methods. Springer International Publishing, Switzerland.

Kowalczyk-Gajewska, K., 2010. Modelling of texture evolution in metals accounting for lattice reorientation due to twinning. Eur. J. Mech. A Solids 29, 28–41.

Levitas, V.I., 1998. Thermomechanical theory of martensitic phase transformations in inelastic materials. Int. J. Solids Struct. 35, 889–940.

Levitas, V.I., Javanbakht, M., 2011. Phase-field approach to martensitic phase transformations: Effect of martensite–martensite interface energy. Int. J. Mat. Res. 102, 652–665.

Levitas, V.I., Preston, D.L., 2005. Thermomechanical lattice instability and phase field theory of martensitic phase transformations, twinning and dislocations at large strains. Phys. Lett. A 343, 32–39.

Li, N., Yang, L., Wang, C., Monclús, M.A., Shi, D., Molina-Aldareguía, J.M., 2021. Deformation mechanisms of basal slip, twinning and non-basal slips in Mg–Y alloy by micropillar compression. Mater. Sci. Eng. A 819, 141408.

Liu, H., Lin, F.X., Zhao, P., Moelans, N., Wang, Y., Nie, J.F., 2018a. Formation and autocatalytic nucleation of co-zone $\{10\bar{1}2\}$ deformation twins in polycrystalline Mg: A phase field simulation study. Acta Mater. 153, 86–107.

Liu, C., Shanthraj, P., Diehl, M., Roters, F., Dong, S., Dong, J., Ding, W., Raabe, D., 2018b. An integrated crystal plasticity–phase field model for spatially resolved twin nucleation, propagation, and growth in hexagonal materials. Int. J. Plast. 106, 203–227.

Liu, C., Shanthraj, P., Robson, J.D., Diehl, M., Dong, S., Dong, J., Ding, W., Raabe, D., 2019. On the interaction of precipitates and tensile twins in magnesium alloys. Acta Mater. 178, 146–162.

Luan, Q., Britton, T.B., Jun, T.-S., 2018. Strain rate sensitivity in commercial pure titanium: The competition between slip and deformation twinning. Mater. Sci. Eng. A 734, 385–397.

Lynch, P.A., Kunz, M., Tamura, N., Barnett, M.R., 2014. Time and spatial resolution of slip and twinning in a grain embedded within a magnesium polycrystal. Acta Mater. 78, 203–212.

Ma, R., Sun, W.C., 2021. Phase field modeling of coupled crystal plasticity and deformation twinning in polycrystals with monolithic and splitting solvers. Int. J. Numer. Methods Engrg. 122, 1167–1189.

Mahajan, S., Williams, D.F., 1973. Deformation twinning in metals and alloys. Int. Metall. Rev. 18, 43–61.

Mareau, C., Daymond, M.R., 2016. Micromechanical modelling of twinning in polycrystalline materials: Application to magnesium. Int. J. Plast. 85, 156–171.

Miehe, C., 1996. Exponential map algorithm for stress updates in anisotropic multiplicative elastoplasticity for single crystals. Int. J. Numer. Methods Engrg. 39, 3367–3390.

Pei, Z., Sheng, H., Zhang, X., Li, R., Svendsen, B., 2018. Tunable twin stability and an accurate magnesium interatomic potential for dislocation-twin interactions. Mat. Des. 153, 232–241.

Pei, Z., Zhang, X., Hickel, T., Friák, M., Sandlöbes, S., Dutta, B., Neugebauer, J., 2017. Atomic structures of twin boundaries in hexagonal close-packed metallic crystals with particular focus on Mg. Npj Comput. Mat. 3, 1–7.

Petryk, H., 2020. A quasi-extremal energy principle for non-potential problems in rate-independent plasticity. J. Mech. Phys. Solids 136, 103691.

Qiao, H., Barnett, M.R., Wu, P.D., 2016. Modeling of twin formation, propagation and growth in a Mg single crystal based on crystal plasticity finite element method. Int. J. Plast. 86, 70–92.

Rezaee-Hajidehi, M., Stupkiewicz, S., 2021. Micromorphic approach to phase-field modeling of multivariant martensitic transformation with rate-independent dissipation effects. Int. J. Solids Struct. 222, 111027.

Rezaee-Hajidehi, M., Tůma, K., Stupkiewicz, S., 2021. A note on Padé approximants of tensor logarithm with application to Hencky-type hyperelasticity. Comput. Mech. 68, 619–632.

Robson, J.D., Stanford, N., Barnett, M.R., 2013. Effect of precipitate shape and habit on mechanical asymmetry in magnesium alloys. Metall. Mat. Trans. A 44, 2984–2995.

Rockafellar, R.T., 1970. Convex Analysis. Princeton University Press, Princeton, New Jersey.

Roters, F., Eisenlohr, P., Hantcherli, L., Tjahjanto, D.D., Bieler, T.R., Raabe, D., 2010. Overview of constitutive laws, kinematics, homogenization and multiscale methods in crystal plasticity finite-element modeling: Theory, experiments, applications. Acta Mater. 58, 1152–1211.

Shi, D., Liu, T., Wang, T., Hou, D., Zhao, S., Hussain, S., 2017. $\{10-12\}$ Twins across twin boundaries traced by in situ EBSD. J. Alloys Compd. 690, 699–706.

Slutsky, L.J., Garland, C.W., 1957. Elastic constants of magnesium from 4.2 K to 300 K. Phys. Rev. 107, 972.

Staroselsky, A., Anand, L., 2003. A constitutive model for hcp materials deforming by slip and twinning: application to magnesium alloy AZ31B. Int. J. Plast. 19, 1843–1864.

Steinbach, I., 2009. Phase-field models in materials science. Model. Simul. Mat. Sci. Eng. 17, 073001.

Stupkiewicz, S., Petryk, H., 2013. A robust model of pseudoelasticity in shape memory alloys. Int. J. Numer. Methods Engrg. 93, 747–769.

Tůma, K., Rezaee-Hajidehi, M., Hron, J., Farrell, P., Stupkiewicz, S., 2021. Phase-field modeling of multivariant martensitic transformation at finite-strain: computational aspects and large-scale finite-element simulations. Comput. Methods Appl. Mech. Engrg. 377, 113705.

Tůma, K., Stupkiewicz, S., Petryk, H., 2016. Size effects in martensitic microstructures: Finite-strain phase field model versus sharp-interface approach. J. Mech. Phys. Solids 95, 284–307.

Tůma, K., Stupkiewicz, S., Petryk, H., 2018. Rate-independent dissipation in phase-field modelling of displacive transformations. J. Mech. Phys. Solids 114, 117–142.

Van Houtte, P., 1978. Simulation of the rolling and shear texture of brass by the taylor theory adapted for mechanical twinning. Acta Metall. 26, 591–604.

Wang, L., Barabash, R., Bieler, T., Liu, W., Eisenlohr, P., 2013. Study of $\{11\bar{2}1\}$ twinning in α-Ti by EBSD and laue microdiffraction. Metall. Mat. Trans. A 44, 3664–3674.

Wang, Y., Chen, L.-Q., Liu, Z.-K., Mathaudhu, S.N., 2010a. First-principles calculations of twin-boundary and stacking-fault energies in magnesium. Scripta Mat. 62, 646–649.

Wang, J., Hoagland, R.G., Hirth, J.P., Capolungo, L., Beyerlein, I.J., Tomé, C.N., 2009. Nucleation of a $(\bar{1}012)$ twin in hexagonal close-packed crystals. Scripta Mat. 61, 903–906.

Wang, J.-Y., Li, N., Alizadeh, R., Monclús, M.A., Cui, Y.W., Molina-Aldareguía, J.M., LLorca, J., 2019. Effect of solute content and temperature on the deformation mechanisms and critical resolved shear stress in Mg-Al and Mg-Zn alloys. Acta Mater. 170, 155–165.

Wang, H., Raeisinia, B., Wu, P.D., Agnew, S.R., Tomé, C.N., 2010b. Evaluation of self-consistent polycrystal plasticity models for magnesium alloy AZ31B sheet. Int. J. Solids Struct. 47, 2905–2917.

Wang, B., Shi, J., Ye, P., Deng, L., Wang, C., Chen, J., Yang, X., Li, Q., 2018. In-situ investigation on nucleation and propagation of $\{10-12\}$ twins during uniaxial multi-pass compression in an extruded AZ31 Mg alloy. Mater. Sci. Eng. A 731, 71–79.

Yaddanapudi, K., Leu, B., Kumar, M.A., Wang, X., Schoenung, J.M., Lavernia, E.J., Rupert, T.J., Beyerlein, I.J., Mahajan, S., 2021. Accommodation and formation of $\{\bar{1}012\}$ twins in Mg-Y alloys. Acta Mater. 204, 116514.

Yoo, M.H., Lee, J.K., 1991. Deformation twinning in h.c.p. metals and alloys. Phil. Mag. A 63, 987–1000.

Yu, Q., Wang, J., Jiang, Y., McCabe, R.J., Li, N., Tomé, C.N., 2014. Twin–twin interactions in magnesium. Acta Mater. 77, 28–42.

Zhang, J., Joshi, S.P., 2012. Phenomenological crystal plasticity modeling and detailed micromechanical investigations of pure magnesium. J. Mech. Phys. Solids 60, 945–972.